

## Melt solidification and late-stage evaporation in the evolution of a FUN inclusion from the Vigarano C3V chondrite

ANDREW M. DAVIS,<sup>1</sup> GLENN J. MACPHERSON,<sup>2</sup> ROBERT N. CLAYTON,<sup>1,3,4</sup> TOSHIKO K. MAYEDA,<sup>1</sup> PAUL J. SYLVESTER,<sup>3</sup> LAWRENCE GROSSMAN,<sup>1,3</sup> RICHARD W. HINTON,<sup>1,\*</sup> and JOHN R. LAUGHLIN<sup>4</sup>

<sup>1</sup>Enrico Fermi Institute, University of Chicago, Chicago, IL 60637, USA

<sup>2</sup>Department of Mineral Sciences, National Museum of Natural History, Smithsonian Institution, Washington, DC 20560, USA

<sup>3</sup>Department of the Geophysical Sciences, University of Chicago, Chicago, IL 60637, USA

<sup>4</sup>Department of Chemistry, University of Chicago, Chicago, IL 60637, USA

(Received March 26, 1990; accepted in revised form November 29, 1990)

**Abstract**—Vigarano 1623-5 is a forsterite-bearing refractory inclusion in which oxygen, magnesium, and silicon show large degrees of mass-dependent isotopic fractionation. The core of 1623-5 consists of forsteritic olivine, fassaite, melilite ( $\text{Åk}_{89}$ ), and spinel, all of which show isotopic mass fractionation, averaging  $\sim 30.6\%$ /amu for magnesium and  $\sim 10.0\%$ /amu for silicon; it is enclosed in a mantle consisting of aluminous melilite ( $\text{Åk}_{16-60}$ ), spinel, perovskite, and hibonite. Hibonite and spinel in the mantle are enriched in heavy isotopes of magnesium by 8–15%/amu relative to the core. 1623-5 originally formed by solidification of a magnesium-rich melt. The endemic isotopic mass fractionation may have been caused by evaporation of that melt or may reflect an earlier evaporation event affecting the reservoir from which the interior of 1623-5 formed. Later flash remelting of the outer part of the core, and volatilization of  $\text{SiO}_2$  and  $\text{MgO}$  from the melt so produced, caused formation of a mantle that is in isotopic and petrologic disequilibrium with the core.

### INTRODUCTION

A SMALL SUBSET OF refractory inclusions in carbonaceous chondrites contain mass fractionated oxygen, magnesium, and silicon and ubiquitous nuclear isotopic anomalies—the so-called FUN inclusions. On the basis of isotopic compositions of oxygen, magnesium, and other elements, five of these peculiar objects have previously been identified, all from the Allende C3V meteorite. We previously reported isotopic (CLAYTON et al., 1987) data for a Vigarano inclusion (USNM 1623-5) that showed it to be the sixth member of this group. Subsequent work (MACPHERSON et al., 1987; DAVIS and MACPHERSON, 1988) has shown this object to be important in another respect, because it shows the first unequivocal correlated petrologic and isotopic evidence for volatilization in a refractory inclusion. We present here the results of a detailed petrologic, chemical, and isotopic study of this unique inclusion.

### ANALYTICAL TECHNIQUES

1623-5 is one of a number of Vigarano inclusions that were sampled for bulk chemical and isotopic analyses and for thin sectioning. On a slab surface, this white inclusion was crudely elliptical in shape and about 4 mm long. The inclusion was split nearly in half, with one portion taken for thin section preparation and the rest sampled for bulk analysis.

The thin section was examined with petrographic and scanning electron microscopes (SEM). The SEMs used were a JEOL JSM-35 equipped with a Kevex 7077 energy dispersive X-ray microanalysis system at the University of Chicago and a JEOL 840A equipped with a Kevex 8000 X-ray microanalysis system at the Smithsonian Insti-

tion. All SEM photographs in this paper are backscattered electron (BSE) images.

Electron microprobe analyses were obtained using two instruments. The electron microprobe at the University of Chicago is an automated Cameca SX-50, equipped with four wavelength dispersive (WD) spectrometers and a Kevex energy dispersive X-ray detector. WD analyses using this instrument were collected using a 15 kV accelerating potential and a beam current of 30 nA. Data from the Cameca probe were reduced via the modified ZAF correction procedure PAP. The electron microprobe at the Smithsonian Institution is an ARL-SEMQ, equipped with six fixed and three adjustable WD spectrometers. This machine was operated with a 15 kV accelerating potential and a 150 nA beam current. Data from the Smithsonian probe were reduced according to the procedure of BENCE and ALBEE (1968).

Trace element contents and magnesium and silicon isotopic compositions in individual phases were analyzed using a modified AEI IM-20 ion microprobe at the University of Chicago. The trace element analysis method was a modified version of that given by HINTON et al. (1988), who measured trace elements other than REEs without using energy filtering to reduce interferences. In this work, energy filtering was used for all elemental analyses. Ion yields were measured under the same conditions in a variety of synthetic and natural silicate minerals and glasses. The methods for isotopic analysis of magnesium are given by HINTON and BISCHOFF (1984). A modified version of the method given by CLAYTON et al. (1984) was used for those silicon isotopic analyses made by ion microprobe: in order to reduce variability in instrumental mass fractionation, energy filtering was used.  $^{29}\text{Si}$  analyses are not reported because of interference from  $^{28}\text{SiH}$ ; the interference of  $^{29}\text{SiH}$  on  $^{30}\text{Si}$  was  $<1\%$ .

Bulk oxygen and silicon isotopic analyses were done on aliquots of powder removed from the facing piece of 1623-5 using a stainless steel dental tool. The oxygen and silicon isotopic analyses were made using the methods given by CLAYTON et al. (1984).

Bulk major and trace elements were analyzed by instrumental neutron activation analysis (INAA) using methods described by MAO et al. (1990). Major elements were determined via rabbit irradiation of an 11.9  $\mu\text{g}$  sample, consisting of only about six grains. A portion of the sample was lost during transfer into a supersilica vial for the long irradiation; after transfer the sample weighed  $8.2 \pm 0.1 \mu\text{g}$ . Corrections for lanthanum interference on cerium (4%), europium interference on samarium (0.4%), tantalum interference on thulium (11%), and ytterbium interference on lutetium (4%) were made by

\* Present address: Grant Institute, Department of Geology and Geophysics, University of Edinburgh, West Mains Road, Edinburgh EH9 3JW, Scotland.

the procedure described by MAO et al. (1990). Despite the small sample size, blank corrections were  $\leq 5\%$ , except for  $^{141}\text{Ce}$  (6%),  $^{140}\text{La}$  (8%),  $^{28}\text{Al}$  (10%),  $^{51}\text{Ti}$  (15%), and  $^{56}\text{Mn}$  (51%).

#### DESCRIPTION

A BSE photomicrograph and accompanying line drawing of 1623-5 are shown in Fig. 1. The portion of 1623-5 present in the thin section is roughly 4 mm long and just under 1.5 mm wide. There are two major pieces, separated by 150–250  $\mu\text{m}$  of intervening matrix. In addition, many smaller fragments occur in the matrix immediately adjoining both parts of the inclusion. The largest piece of 1623-5 in the section

has a structure dominated by a large, nearly spherical reentrant that is filled with meteorite matrix. This structure is very similar to one seen previously in the Allende inclusion ALVIN and which was interpreted by MACPHERSON et al. (1981, 1985) to be a vesicle.

The interior portion of 1623-5, composed of olivine, fassaite, and åkermanitic melilite, constitutes the major portion of the inclusion. Overlying the core is an  $\sim 200 \mu\text{m}$  thick, discontinuous melilite-rich mantle. This mantle occurs in two mineralogically and texturally distinct types, depending on whether the underlying core is composed of melilite and olivine or fassaite and olivine.

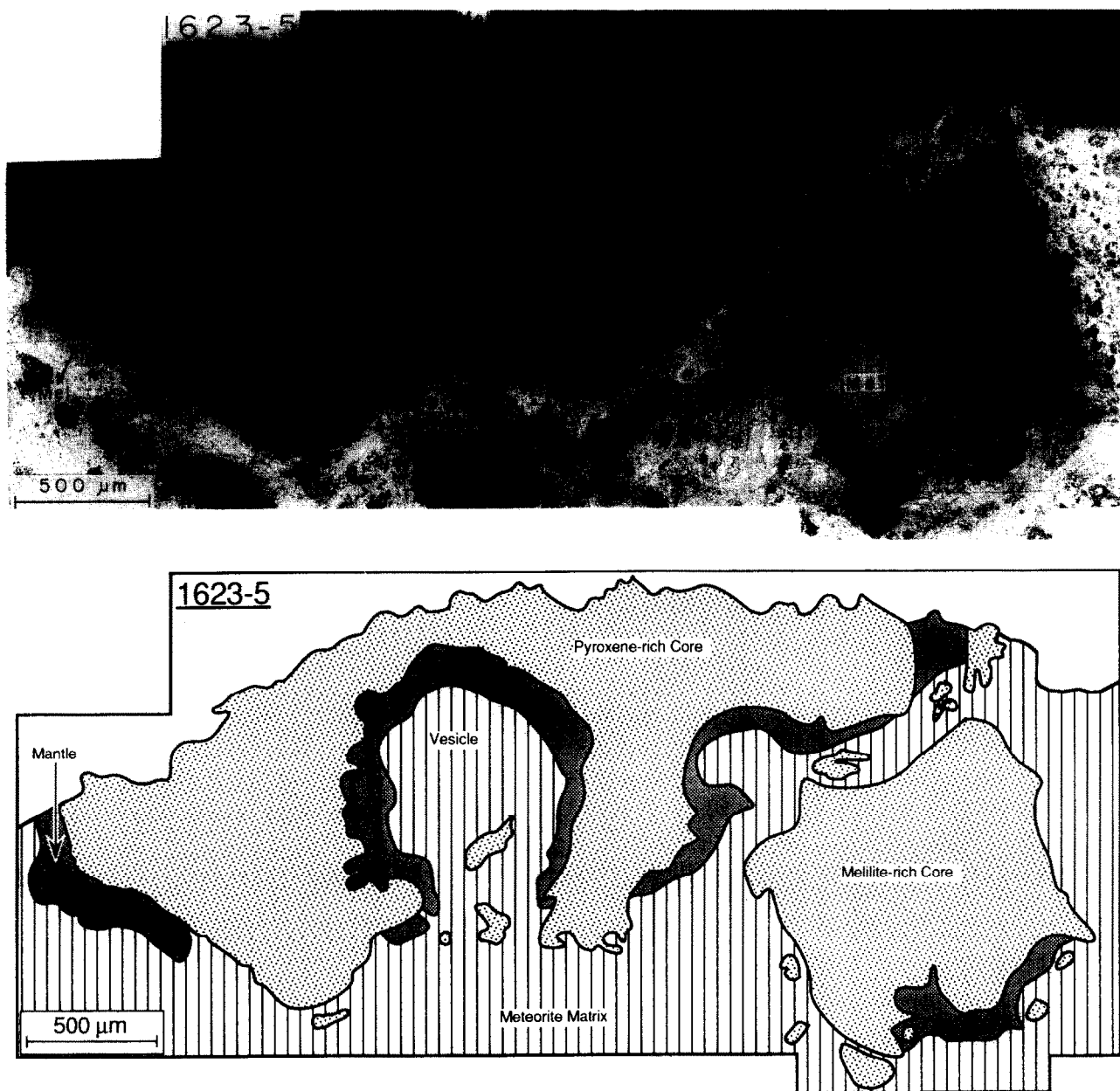


FIG. 1. (a) Backscattered electron (BSE) photomicrograph of a thin section of 1623-5. "Y-Z" marks the location of the electron microprobe traverse shown in Fig. 10. (b) Line drawing of the photograph in (a), showing the locations of the major structural features of 1623-5.

## Core

The core (Fig. 1) consists mostly of equant 30–170  $\mu\text{m}$  olivine crystals poikilitically enclosed within 200–500  $\mu\text{m}$  fassaite and melilite crystals. Olivine crystals enclosed within fassaite are euhedral to subhedral in shape, but those within melilite are rounded and tend to be somewhat smaller in size; this difference may be due to a reaction relationship between olivine and liquid that produces melilite (see Discussion). The fassaite and melilite are inhomogeneously distributed: in the larger portion of 1623-5 shown in Fig. 1 fassaite is much more abundant than melilite; in the smaller portion there is very little fassaite. Spinel is a minor phase in the core: 5–20  $\mu\text{m}$  grains are heterogeneously distributed throughout as inclusions within all other phases, and clusters of grains (“framboids”) are commonly enclosed within fassaite. These textures indicate that the order of appearance of phases in the core was spinel first, followed by olivine, and finally fassaite and melilite in uncertain relative order. Excluding the mantle, the approximate modal ( $\sim$  volume) proportions of the phases in bulk 1623-5, determined by point-counting, are 52% olivine, 16% pyroxene, 7% spinel, and 26% melilite.

Olivine and spinel both show intense cathodoluminescence under electron bombardment. All olivine in the core is extremely low in iron and shows a strong blue luminescence. Along grain boundaries and cracks, olivine is more iron-rich and shows no visible cathodoluminescence. Similarly, low-iron spinel enclosed within olivine shows a distinctive bright red luminescence while iron-bearing spinel near cracks and along alteration veins shows no visible cathodoluminescence. Cathodoluminescence photography of the inclusion thus reveals the distribution of iron within the inclusion and indicates that the iron is secondary in origin: iron enrichment is most pronounced near fractures and along grain boundaries, and iron-enriched cracks and grain boundaries are more numerous towards the outside of the inclusion.

Alteration in this inclusion is relatively minor, similar to other Vigarano coarse-grained inclusions but in contrast to those from Allende. In addition to enrichments in iron and sodium in the major phases near the inclusion margin (see Mineral Chemistry) and along fractures, the principal manifestations of alteration are veins of calcite and an unknown, silica-rich phase that preferentially replaces åkermanitic melilite.

## Melilite Mantle over Melilite-Olivine Core

In the area of melilite mantle overlying melilite and olivine at one end of 1623-5 (lower left in Fig. 1) the mantle consists predominantly of relatively aluminum-rich melilite that contrasts strongly with the åkermanitic variety in the inclusion interior. An aluminum  $K_{\alpha}$  X-ray map (Fig. 2) shows that the mantle has a sharp but somewhat irregular boundary with the inclusion core. Where the melilite mantle overlies an area of olivine poikilitically enclosed in Åk<sub>89</sub> melilite, there is a 50  $\mu\text{m}$  wide band in which olivine is pseudomorphically replaced by nearly pure åkermanite. These pseudomorphs are invisible with an optical microscope or with BSE imaging (Fig. 2a), but are clearly visible in the aluminum X-ray map (Fig. 2b); there can be little doubt from the texture that olivine

has been replaced by åkermanite. In this area, rounded areas of nearly pure åkermanite are poikilitically enclosed in Åk<sub>89</sub> melilite. One such olivine “ghost” can be seen in Fig. 3, between the traverses marked K–L and M–N on Fig. 2. This grain actually straddles the mantle-core boundary, so that a relict portion of the original olivine grain is preserved on the “core” end; the relict grain is half-moon shaped (Fig. 3a), and its curvature and position conform exactly to those of the ghost that is visible on the X-ray map in Fig. 3b. The åkermanite ghosts enclose tiny randomly dispersed spinel grains, just as interior olivine does. Spinel grains are sporadically distributed throughout the mantle, and, significantly, near the outermost edge of the mantle there are rare small grains of hibonite (Fig. 4). The discovery of hibonite in this inclusion was unexpected, as the bulk inclusion is rather depleted in aluminum relative to other refractory inclusions. The hibonite occurs as scattered grains only in the outermost parts of the melilite mantle overlying the melilite-olivine core (Fig. 4) and in the porous portion of the melilite mantle overlying the fassaite-olivine core (described below). As will be discussed below, an assemblage containing aluminous melilite

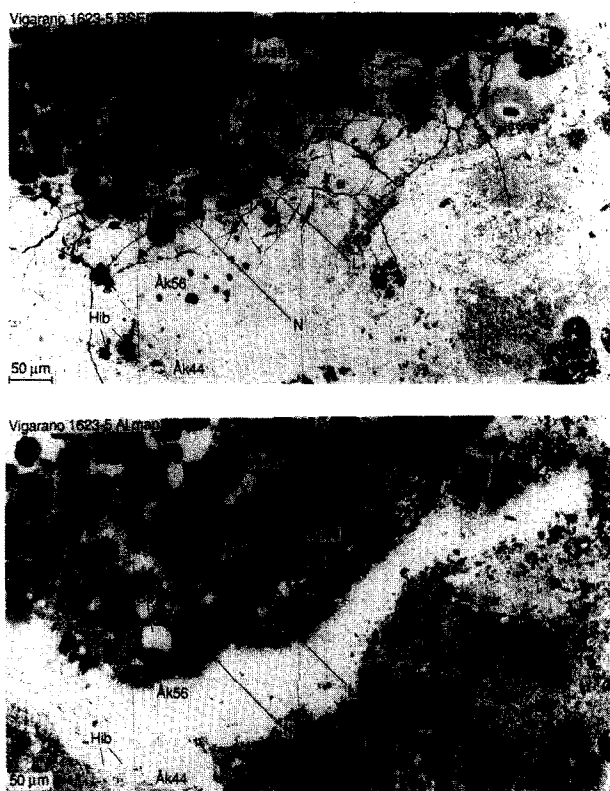


FIG. 2. (a) BSE photomicrograph of a portion of the olivine-free melilite mantle of 1623-5 that overlies a forsterite-melilite-rich core. M–N and K–L mark the locations of electron microprobe traverses shown in Fig. 11. Note that several of the large olivine crystals nearest the edge of the mantle are incomplete (“half-round”). (b) Aluminum X-ray map of the region shown in (a). The mantle consists of melilite in the composition range Åk<sub>56</sub>–Åk<sub>44</sub> and is thus very Al-rich relative to the interior in which the melilite is Åk<sub>85</sub>. Note that many of the incomplete olivines in (a) now appear to be whole, because they are attached to pseudomorph “ghosts” of nearly pure åkermanite (Åk<sub>89</sub>). Abbreviations: Åk = åkermanite; Fo = forsteritic olivine; Hib = hibonite; Sp = spinel.

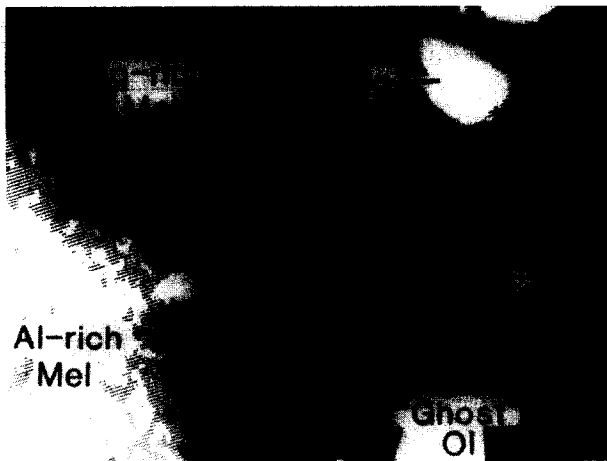
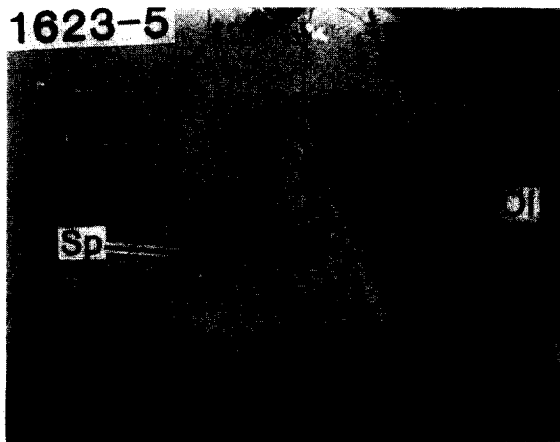


FIG. 3. (a) BSE photomicrograph of half-round forsterite grain partially replaced by a "ghost" of nearly pure åkermanite. (b) Aluminum X-ray map of the region shown in (a). The åkermanitic "ghost" is not visible in the BSE image but can be clearly seen in the X-ray map.

+ spinel + hibonite (e.g., the mantle) is totally out of equilibrium with one containing forsterite + magnesium-rich melilite (e.g., the core).

#### Melilite Mantle over the Fassaite-Olivine Core

The portions of mantle that overlie the fassaite-rich core are best exposed along the surface of 1623-5 inside the large vesicle indicated on Fig. 1. The BSE photomicrograph in Fig. 5 shows that this mantle is characterized by a discontinuous band, 10–25  $\mu\text{m}$  thick and in contact with fassaite, that consists of a symplectitic intergrowth of melilite plus fine-grained vermiform perovskite. The intergrowth embays the fassaite, thus producing a highly scalloped boundary. A few of the wormy perovskites extend for a few microns into the fassaite, but, for the most part, the fassaite contains no perovskite. Within the symplectite, perovskite is commonly oriented in a subradial fashion (Fig. 5) perpendicular to the surface of the fassaite interface. The textures of this boundary zone clearly indicate that the fassaite has been replaced by the melilite and perovskite; the textures within the symplectite

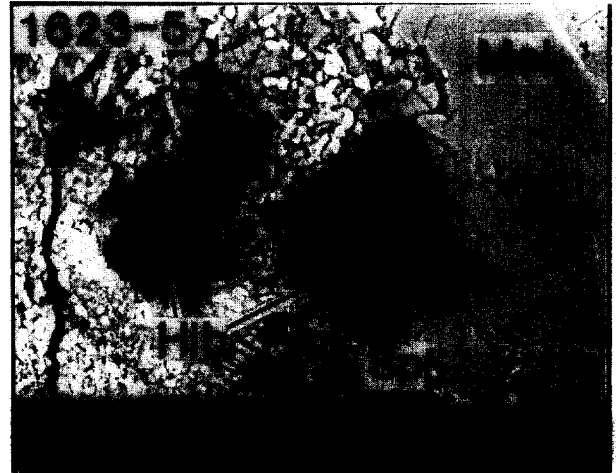


FIG. 4. BSE photomicrograph of intergrown hibonite and spinel in the mantle of 1623-5. Contrary to the more common case, the hibonite here appears darker than the spinel in BSE imaging because of the high iron content of the spinel. Abbreviations: Mel = melilite; others as used previously.

itself suggest either rapid crystallization from a liquid or devitrification of a glass.

Outside the melilite-perovskite band is a porous band, up to 100  $\mu\text{m}$  thick, that consists largely of <1–5  $\mu\text{m}$  grains of gehlenitic melilite and perovskite. Dispersed within the porous band are 10–20  $\mu\text{m}$  spinel grains. In places, oriented clusters of vermiform perovskite crystals within the porous mantle resemble those in the gehlenite-perovskite band that overlies fassaite. As shown in the BSE photo and Ti X-ray map in Fig. 6, the boundary between the porous part of the melilite-rich mantle and the meteorite matrix within the spheroidal reentrant (vesicle) parallels the shape of the cavity; although not visible in Fig. 6, the contact is commonly marked by euhedral crystals of andradite. This phase has previously been found in accretionary rims in CAIs (MACPHERSON et al., 1985). A step-scan profile across this mantle (Fig. 7; the location is marked S-T on Fig. 6) shows that  $\text{TiO}_2$  rises abruptly

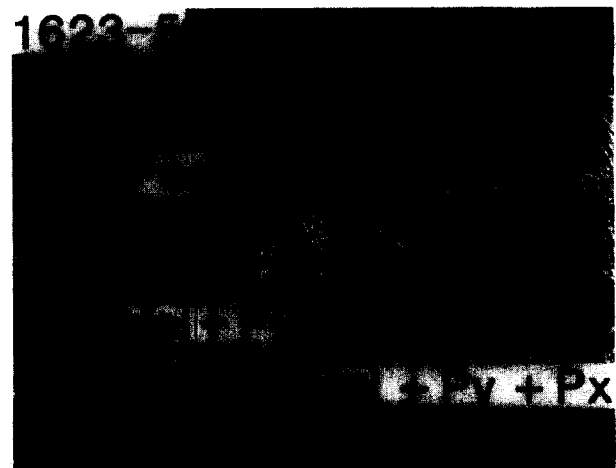


FIG. 5. BSE photomicrograph of intergrown melilite and perovskite overlying fassaite in the mantle of 1623-5, located along the interior of the large vesicle indicated in Fig. 1.

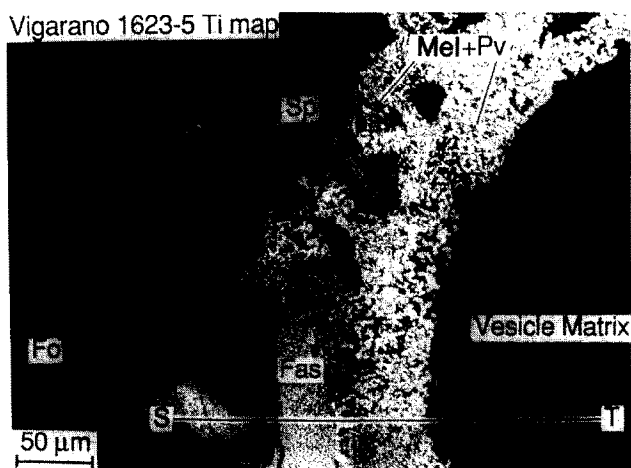
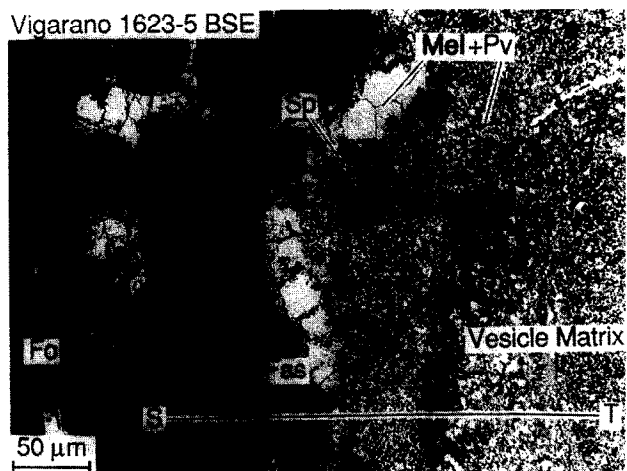


FIG. 6. BSE photomicrograph (a) and titanium X-ray map (b) of the mantle and meteorite matrix overlying part of the core of 1623-5, along the interior of the large vesicle indicated in Fig. 1. Note that the porous mantle is very enriched in titanium (perovskite) and that the boundary between the porous mantle and the matrix follows a smooth curve that parallels the wall of the vesicle itself; this porous mantle/matrix boundary was probably the original wall of the vesicle prior to the volatilization event that led to the formation of the porous mantle. S-T marks the location of the electron microprobe traverse shown in Fig. 7. Abbreviations as used previously except: Fas = fassaite; Geh = gehlenite-rich melilite.

in passing from core forsterite to fassaite, falls off gradually from about 5–6% in the fassaite except where it drops sharply in a spinel grain, fluctuates through the region of spinel + melilite intergrowth and porous mantle, then falls to ~0.1% within the meteorite matrix. CaO indicates the presence of olivine (1.7% CaO), fassaite (25% CaO), and melilite (40% CaO). The CaO content of meteorite matrix next to the porous matrix is quite high and reflects the presence of andradite.

#### MINERAL CHEMISTRY

##### Forsterite

Representative analyses of forsterite are given in Table 1. The most characteristic chemical feature is ~1.7 wt% CaO; such high calcium contents are a hallmark of olivines in for-

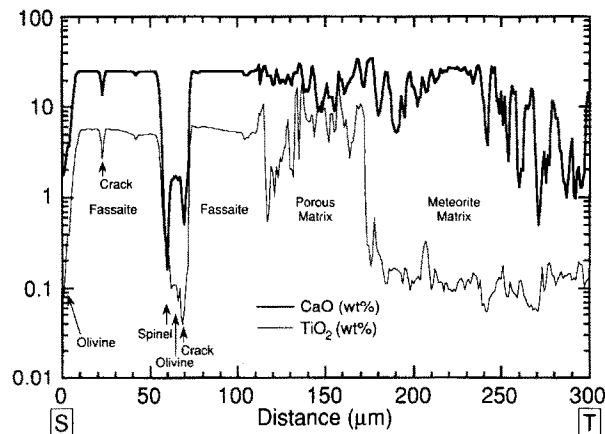


FIG. 7. Electron microprobe step-scan S-T across the contact between fassaite-rich core, nonporous mantle and porous mantle, and meteorite matrix. Location of traverse is shown on Fig. 6. See text for discussion.

sterite-bearing inclusions (DOMINIK et al., 1978; CLAYTON et al., 1984; WARK et al., 1987) and reflect the high temperatures of formation and unusual bulk compositions of these inclusions (CLAYTON et al., 1984). These olivines are otherwise exceedingly pure forsterites, with other elements (Al, Cr, Fe, Ti) present at levels rarely exceeding 0.1 wt%. Along fractures and grain margins, however, FeO concentrations can be as high as 1.5 wt%; these higher FeO contents are probably the result of secondary alteration processes.

##### Fassaite

Representative analyses of fassaite are given in Table 2. The range of  $Al_2O_3$  and  $TiO_2$  contents of 1623-5 fassaite is shown in Fig. 8. The levels of these elements are similar to those found in Type B2 inclusions (e.g., WARK and LOWERING, 1982) and in other forsterite-bearing inclusions (e.g., CLAYTON et al., 1984; DOMINIK et al., 1978; WARK et al., 1987); one exception to the latter is the Allende inclusion 818 (WARK et al., 1987) in which pyroxene is markedly lower in  $TiO_2$  than that in 1623-5. The marked bimodal distribution of  $Al_2O_3$  contents in Fig. 8 reflects compositional sector-zoning of fassaite in 1623-5.

About one-third of the titanium in 1623-5 fassaite is trivalent. Figure 9 is a plot of titanium atoms vs. total cations (both per six oxygens) for fassaite, for which the data were calculated assuming that all titanium is tetravalent. With only

Table 1. Electron microprobe analyses of forsterite (in wt%).

	26-16	26-27	8-17
SiO <sub>2</sub>	42.40	42.76	41.81
Al <sub>2</sub> O <sub>3</sub>	0.06	0.07	0.06
TiO <sub>2</sub>	0.08	0.08	0.06
MgO	55.62	55.87	55.43
FeO	0.05	0.05	0.02
CaO	1.69	1.72	1.69
Cr <sub>2</sub> O <sub>3</sub>	*n.d.	n.d.	n.d.
V <sub>2</sub> O <sub>3</sub>	0.01	n.d.	0.01
Total	99.91	100.55	99.08

\*n.d.—not detected, <0.01 wt%.

Table 2. Electron microprobe analyses of fassaite (in wt%).

	P4	P9	P37	EF-7	P53
SiO <sub>2</sub>	47.40	47.33	41.38	39.82	36.27
Al <sub>2</sub> O <sub>3</sub>	11.15	9.94	16.98	17.66	22.83
TiO <sub>2</sub> *	2.90	3.82	5.53	6.04	7.82
MgO	14.22	14.52	11.52	11.51	8.53
FeO	0.03	0.03	0.04	0.03	0.15
CaO	24.80	24.92	24.64	25.40	25.03
Na <sub>2</sub> O	†n.d.	n.d.	n.d.	n.d.	n.d.
MnO	n.d.	n.d.	n.d.	0.01	0.01
Cr <sub>2</sub> O <sub>3</sub>	n.d.	0.01	0.03	0.04	0.07
V <sub>2</sub> O <sub>3</sub>	n.d.	0.05	0.06	0.08	0.16
Sc <sub>2</sub> O <sub>3</sub>	n.d.	0.11	0.06	0.10	0.03
Y <sub>2</sub> O <sub>3</sub>	0.02	n.d.	n.d.	0.01	0.02
ZrO <sub>2</sub>	0.02	0.03	0.04	0.04	0.05
Total	100.54	100.76	100.28	100.74	100.97

\*Total Ti as TiO<sub>2</sub>. †n.d.—not detected, <0.01 wt%.

three exceptions, the analyses show less than four cations per formula unit (the same results were obtained with both electron probes, by different analysts using different standard sets). This relationship implies that some of the titanium (the only abundant multivalent element) must be trivalent. Plots of the type shown in Fig. 9 have the property that constant values of the ratio  $Ti^{+3}/(Ti^{+3} + Ti^{+4})$  are defined by straight lines passing through four cations per six oxygens at zero titanium per six oxygens. Several such lines, corresponding to a range of  $Ti^{+3}/(Ti^{+3} + Ti^{+4})$  values, are plotted in Fig. 9. More than half of the data fall in the range of 0.2 to 0.4 for this ratio. Although the errors in calculating the values plotted in Fig. 9 are large because the total titanium content of 1623-5 fassaite is low, the data suggest that approximately 30% of the titanium in 1623-5 is trivalent. Most of the analyses plotted in Fig. 9 are from the core of the inclusion. However, 16 of the analyzed fassaite are located in the region immediately underlying the melilite-perovskite portion of the melilite-rich mantle (shown in Fig. 5); 9 of these plot between  $Ti^{+3}/(Ti^{+3} + Ti^{+4}) = 0$  and 0.2, implying that most or all of the titanium in fassaite next to the mantle is tetravalent.

### Melilite

Representative analyses of melilite are given in Table 3. In the main mass of 1623-5, most of the melilite in the core is of  $\check{A}k_{89}$  composition with little zoning (analysis #131, Table

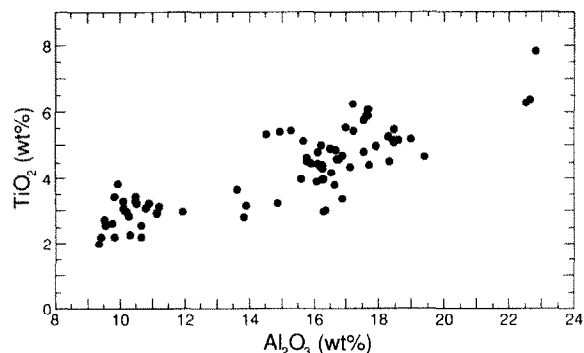


FIG. 8. Al<sub>2</sub>O<sub>3</sub> vs. TiO<sub>2</sub> in fassaite in 1623-5. The marked bimodality that shows most strongly in Al<sub>2</sub>O<sub>3</sub> is the result of compositional sector-zoning in crystals.

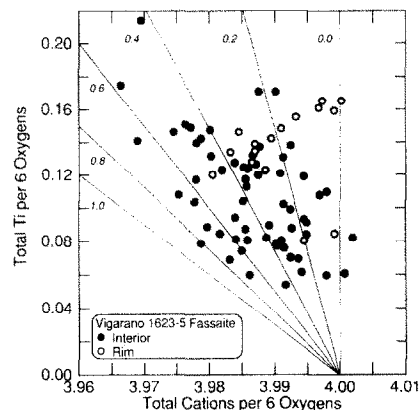


FIG. 9. Ti vs. total cations per six oxygens in 1623-5 fassaite. See text for discussion.

3). Forsterite-free melilite in the smaller of the portions of 1623-5 (on the right side of Fig. 1) is zoned, as shown in the zoning profile in Fig. 10: from a minimum of  $\check{A}k_{65}$  near a spinel at the center of the profile, the  $\check{A}k$  contents increase smoothly outwards and eventually reach  $\check{A}k_{87}$ . Adjacent to olivine, there is a sharp increase from  $\check{A}k_{87}$  to  $\check{A}k_{95}$ . The  $\check{A}k$  zoning is accompanied by more complex zoning in TiO<sub>2</sub>, in which TiO<sub>2</sub> first increases with  $\check{A}k$  content, then drops.

Two step-scan profiles across mantle melilite are plotted in Fig. 11; the locations of these traverses are indicated on Fig. 2. In profile K–L, the traverse extends from a core forsterite grain into  $\check{A}k_{89}$  typical of interior melilite. It then passes into an  $\check{a}k$ ermanite pseudomorph (ghost) of olivine; the change in gehlenite content, from  $\check{A}k_{89}$  to  $\check{A}k_{98}$ , occurs over a distance of only 5  $\mu$ m (CaO profiles, also plotted, clearly distinguish between melilite, which contains ~41 wt% CaO, and olivine, which contains 1.7% CaO). The  $\check{a}k$ ermanite inside of the pseudomorph is uniformly  $\check{A}k_{97-100}$  (analyses #M112 and M120, Table 3). As the traverse passes from the  $\check{a}k$ ermanite ghost out into the melilite mantle, the melilite composition changes from  $\check{A}k_{98}$  to  $\check{A}k_{60}$  over a distance of 20  $\mu$ m. Thereafter, the composition of the mantle melilite gradually changes from  $\check{A}k_{60}$  to  $\check{A}k_{48}$  (at the outermost edge

Table 3. Electron microprobe analyses of melilite (in wt%).

	432	103	113	131	M120	M112
SiO <sub>2</sub>	27.14	31.62	33.68	41.47	43.65	44.01
Al <sub>2</sub> O <sub>3</sub>	28.56	19.92	17.43	4.15	0.74	0.32
TiO <sub>2</sub>	0.08	0.11	0.30	0.10	0.02	0.06
MgO	3.94	5.94	7.11	12.20	14.35	14.73
FeO	0.14	0.66	0.20	0.19	0.22	0.20
CaO	40.09	40.40	40.89	40.81	41.17	41.66
Na <sub>2</sub> O	*n.a.	0.40	0.29	0.14	0.06	0.04
K <sub>2</sub> O	0.02	0.01	0.01	0.01	n.a.	n.a.
MnO	n.a.	n.a.	n.a.	n.a.	0.01	0.01
Cr <sub>2</sub> O <sub>3</sub>	0.02	0.04	0.04	0.05	†n.d.	0.01
V <sub>2</sub> O <sub>3</sub>	0.01	n.a.	n.a.	n.a.	n.d.	n.d.
Sc <sub>2</sub> O <sub>3</sub>	n.a.	n.a.	n.a.	n.a.	n.d.	0.02
Y <sub>2</sub> O <sub>3</sub>	n.a.	n.a.	n.a.	n.a.	n.d.	0.01
ZrO <sub>2</sub>	n.a.	n.a.	n.a.	n.a.	n.d.	n.d.
Total	100.00	99.10	99.95	99.12	100.22	101.07
$\check{A}k^{\ddagger}$	23	46	53	89	98	99

\*n.a.—not analyzed. †n.d.—not detected, <0.01 wt%. ‡ $\check{A}k$ —mole %  $\check{a}k$ ermanite, calculated from Al and Si cations per 7 oxygens.

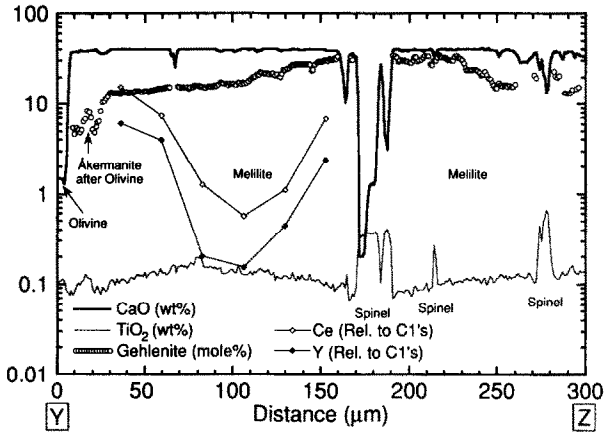


FIG. 10. Step-scan Y-Z across the melilite-rich portion of 1623-5. The location of the traverse is shown on Fig. 1a. See text for discussion.

of the inclusion). The second traverse shown (M-N) starts in core forsterite, passes into an akermanite pseudomorph, then into normal  $\dot{A}k_{89}$  core melilite, and finally into melilite mantle. The akermanite pseudomorph in this case contains 2 mol% gehlenite, and again there is a sharp boundary between  $\dot{A}k_{98}$  and  $\dot{A}k_{89}$  melilite. Where the  $\dot{A}k_{89}$  melilite is di-

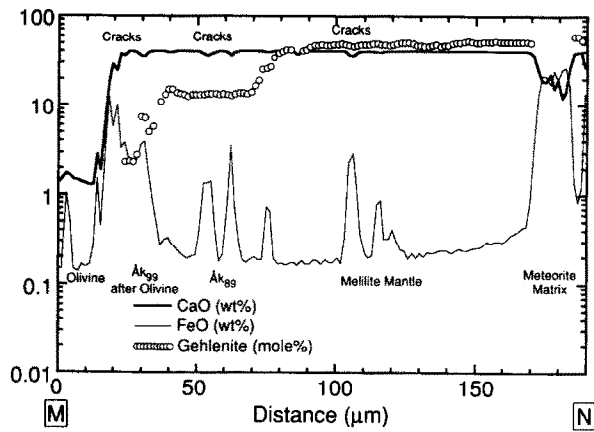
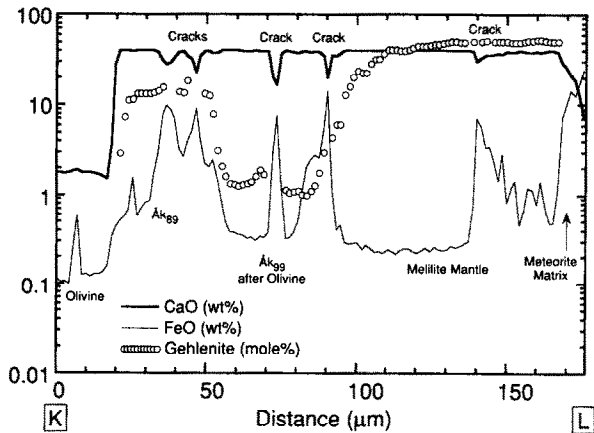


FIG. 11. Step-scans K-L (a) and M-N (b) across the melilite mantle overlying the melilite-rich core of 1623-5. The locations of the traverses are shown on Fig. 2.

rectly in contact with the melilite mantle, the composition changes from  $\dot{A}k_{89}$  to  $\dot{A}k_{60}$  over only 10  $\mu\text{m}$  and the melilite mantle is zoned gradually from  $\dot{A}k_{60}$  to  $\dot{A}k_{47}$ .

A histogram of the melilite compositions in 1623-5 (Fig. 12) shows a distinct trimodal composition, reflecting the different origins of these melilites. The sharp peaks at  $\dot{A}k_{89}$  and  $\dot{A}k_{98}$  represent the normal core melilite and olivine pseudomorphs, respectively, in which there is little compositional variation. The melilite in the compositional range  $\dot{A}k_{<75}$  consists mostly of melilite from the outer mantle, which covers a relatively broad compositional spectrum.

Melilite in the compact mantle overlying fassaite is in the range  $\dot{A}k_{36-63}$  (analyses #103 and 113, Table 3). In the porous portion of the mantle, the range is  $\dot{A}k_{16-43}$  (analysis #432, Table 3).

Although largely unaltered, 1623-5 melilite nonetheless does show the effects of some secondary processes. FeO profiles on Fig. 11 show that FeO contents rise dramatically in cracks, and, in addition, the FeO content of the mantle melilite gradually increases outwards as the inclusion margin is approached, from 0.25 to 0.45 wt%. Sodium in melilite also increases toward the margin of the inclusion. We attribute these enrichments to secondary introduction of sodium and iron into the melilite.

Spinel

Representative analyses of spinel are given in Table 4. CaO and SiO<sub>2</sub> contents average around 0.13 and 0.10 wt%, respectively. FeO contents for most interior spinels, particularly those enclosed within olivine crystals and thus presumably protected from the effects of secondary processes, are generally less than ~0.01 wt%. In contrast, many of the spinels near the outer margins of 1623-5, and even many in the interior that are not enclosed within forsterite crystals, show moderate to large enrichments in iron; crystals bordering the meteorite matrix have been found to contain as much as 15 wt% FeO. FeO and MgO strongly anticorrelate in the spinel, suggesting

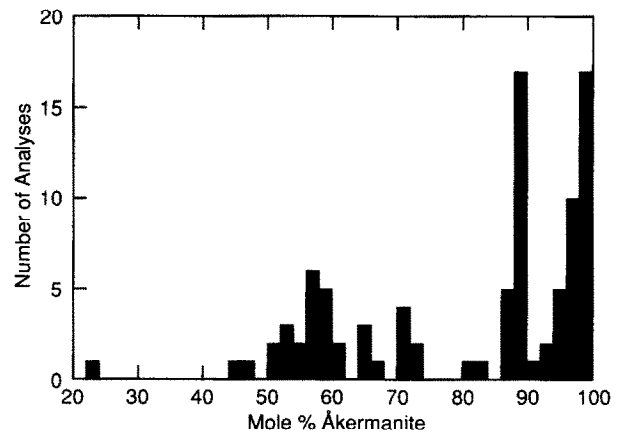


FIG. 12. Histogram of akermanite compositions in 1623-5 melilites. The three peaks correspond to the three different kinds of melilite in the inclusion: nearly pure akermanite that forms pseudomorphs after olivine,  $\dot{A}k_{85}$  that occurs in the inclusion core, and  $\dot{A}k_{<60}$  in the melilite mantle.

Table 4. Electron microprobe analyses of spinel (in wt%).

	437	439	440	403	405
SiO <sub>2</sub>	0.12	0.04	0.03	0.14	0.15
Al <sub>2</sub> O <sub>3</sub>	70.55	70.12	70.66	69.07	64.41
TiO <sub>2</sub>	0.31	0.32	0.01	0.66	0.31
MgO	28.07	27.72	28.10	26.07	17.58
FeO	0.15	0.21	0.41	2.58	15.14
CaO	0.16	0.18	0.10	0.17	0.33
Cr <sub>2</sub> O <sub>3</sub>	0.34	0.31	0.02	0.28	0.09
V <sub>2</sub> O <sub>3</sub>	0.17	0.11	0.29	0.16	0.21
Total	99.87	99.01	99.62	99.13	98.22

437, 439, 440 from interior; 403, 405 from outer part of mantle.

that iron is substituting for magnesium in the spinel structure and therefore is probably present as Fe<sup>2+</sup>.

### Hibonite

Representative hibonite analyses are given in Table 5. Ranges of minor element contents in the hibonite are as follows: TiO<sub>2</sub>, 4.15–5.88 wt%; MgO, 2.24–3.16%; FeO, 0.26–0.57%; V<sub>2</sub>O<sub>3</sub>, 0.21–0.28%; Cr<sub>2</sub>O<sub>3</sub>, 0.02–0.07%.

### ISOTOPIC COMPOSITION

#### Bulk Data

The bulk oxygen isotopic composition of 1623-5 is  $\delta^{17}\text{O} = -23.0\text{‰}$  and  $\delta^{18}\text{O} = -8.3\text{‰}$ . Oxygen data are plotted on a three-isotope diagram in Fig. 13, relative to Standard Mean Ocean Water (SMOW). Compared to the mixing line defined by data for Allende refractory inclusions, the bulk composition of 1623-5 is <sup>18</sup>O-rich, <sup>17</sup>O-poor and plots near the inclusions TE, CG-14, C1, and EK-1-4-1. The isotopic compositions of the latter inclusions have been interpreted as resulting from a mass fractionation event that operated on material having the composition of the extreme <sup>16</sup>O-rich end of the Allende mixing line. Along with the inclusion HAL (LEE et al., 1980), these are the only known inclusions to show such mass fractionation in oxygen. The oxygen isotopic fractionation from the extreme <sup>16</sup>O-rich end of the Allende mixing line is essentially identical in 1623-5 and C1 (Fig. 13). As we will show below, 1623-5 also shares with these other inclusions a strongly mass-fractionated magnesium isotopic signature.

The bulk silicon isotopic composition of 1623-5 is  $\delta^{29}\text{Si} = 10.52\text{‰}$  and  $\delta^{30}\text{Si} = 20.26\text{‰}$ . The only inclusion with a larger silicon mass fractionation is C1 (MOLINI-VELSKO et al., 1983), which has  $\delta^{30}\text{Si} = 28.52\text{‰}$ . The only other inclu-

Table 5. Electron microprobe analyses of hibonite (in wt%).

Sample	409	408
SiO <sub>2</sub>	0.25	0.14
Al <sub>2</sub> O <sub>3</sub>	84.68	82.65
TiO <sub>2</sub>	4.15	5.79
MgO	2.24	3.16
FeO	0.57	0.46
CaO	8.35	8.49
Cr <sub>2</sub> O <sub>3</sub>	0.05	0.06
V <sub>2</sub> O <sub>3</sub>	0.25	0.28
Total	100.54	101.03

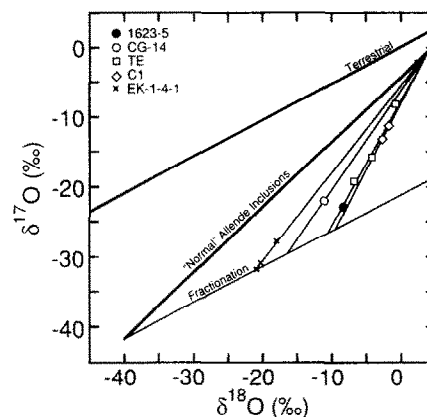


FIG. 13. 3-isotope oxygen diagram showing the mass-fractionated nature of 1623-5 oxygen relative to the normal Allende mixing line. Data for the FUN inclusions C1 and EK-1-4-1 are from CLAYTON and MAYEDA (1977) and for CG-14 and TE are from CLAYTON et al. (1984).

sions with substantial silicon mass fractionations are EK1-4-1, CG14, and TE. MOLINI-VELSKO et al. (1983) determined that on a plot of  $\delta^{29}\text{Si}$  vs.  $\delta^{30}\text{Si}$  nearly all CAIs and chondrules lie along a line passing through the origin and having a slope of 0.5046. After correcting  $\delta^{29}\text{Si}$  for mass fractionation using  $\delta^{30}\text{Si}$  and a slope of 0.5046, there remains an excess of 0.30‰ for  $\delta^{29}\text{Si}$ . This is outside experimental uncertainty of  $\pm \sim 0.1\text{‰}$ . Calculated in the same way, C1 has an excess of 0.46‰ for  $\delta^{29}\text{Si}$ . LOSS et al. (1990a) found that 1623-5 has nuclear isotopic anomalies in magnesium, calcium, titanium, strontium, barium, and samarium and pointed out that the anomalies for each of these elements, along with oxygen, are identical within analytical uncertainty to those in C1. To this list can be added silicon. LOSS et al. (1990b) reported that 1623-5 has a small negative <sup>54</sup>Cr anomaly, only one-third the size of the anomaly in C1 (PAPANASTASSIOU, 1986). As chromium is less refractory than the other elements with nuclear isotope anomalies, some exchange with normal solar system material may have occurred. The agreement in isotopic composition between the two FUN inclusions remains quite remarkable.

#### Ion Microprobe Data for Discrete Phases

The isotopic compositions of magnesium and silicon were measured by ion microprobe in the major individual phases in the core and mantle (Table 6). All interior phases have nearly identical average magnesium isotopic compositions, but silicon is not as isotopically heavy in olivine as it is in melilite and fassaite. Mantle melilite is virtually identical in isotopic composition to interior melilite in magnesium and silicon isotopic composition, whereas spinel and hibonite in the mantle have significantly heavier magnesium than interior phases. Both the porous mantle and the compact melilite-perovskite mantle overlying fassaite-rich portions of the interior have magnesium that is isotopically lighter than interior phases but still quite heavy compared to normal solar system materials (Table 6). The data confirm the preliminary finding of MACPHERSON et al. (1987) that, while all petrologically

Table 6. Magnesium and silicon isotopic composition of phases in Vigarano 1623-5, determined by ion microprobe. Uncertainties given are  $\pm 2\sigma$  standard errors.

Phase	Number of spots	$\Delta^{25}\text{Mg}$ (‰)		$\delta^{26}\text{Mg}$ (‰)	Number of spots	$\delta^{30}\text{Si}$ (‰)
		mean	range			
<i>Interior</i>						
Olivine	38	29.2 $\pm$ 0.4	24.6-35.2	-0.8 $\pm$ 0.8	4	15.2 $\pm$ 7.0
Melilite, $\text{Åk}_{>70}$	19	31.9 $\pm$ 0.3	29.5-35.7	-0.3 $\pm$ 0.9	4	27.1 $\pm$ 5.0
Fassaite	7	33.0 $\pm$ 0.9	31.0-38.3	-1.3 $\pm$ 2.5	3	24.1 $\pm$ 3.8
Spinel	2	31.5 $\pm$ 0.6	31.2-31.8	-3.7 $\pm$ 6.2		
Bulk*		30.6 $\pm$ 0.3		-0.9 $\pm$ 0.7		20.0 $\pm$ 4.2
<i>Mantle</i>						
Melilite, $\text{Åk}_{<70}$	13	32.9 $\pm$ 0.9	28.9-35.0	-1.9 $\pm$ 1.2	1	28.3 $\pm$ 7.4
Spinel	4	38.2 $\pm$ 1.5	36.0-39.4	-3.7 $\pm$ 3.6		
Hibonite	2	45.0 $\pm$ 3.9	43.1-47.0	-4.8 $\pm$ 0.4		
Porous Rim	2	24.3 $\pm$ 0.4	24.1-24.5	-3.4 $\pm$ 5.4		
Melilite-Perovskite	5	28.9 $\pm$ 2.6	24.4-31.7	0.0 $\pm$ 2.3		
All†	96			-1.3 $\pm$ 0.6		

\*Weighted average composition, assuming 52% olivine, 26% melilite, 16% pyroxene and 7% spinel. †Includes 4 analyses that overlapped onto two or more phases.

distinct portions of 1623-5 show enrichments in the heavy isotopes of magnesium and silicon, some phases in both the coherent and porous portions of the melilite mantle show larger degrees of mass fractionation than those in the core. The bulk magnesium and silicon isotopic composition of the interior of 1623-5 was calculated from the modal proportions of the phases and the mean isotopic compositions of phases. The calculated bulk silicon isotopic composition,  $\delta^{30}\text{Si} = 20.0 \pm 4.2\%$ , is in agreement with the value measured by conventional mass spectrometry,  $\delta^{30}\text{Si} = 20.26\%$ .

## CHEMICAL COMPOSITION

### Bulk Analyses

The bulk composition of 1623-5 as determined by INAA is given in Table 7. Ion microprobe analyses of a number of trace elements, including the REEs, in the phases of 1623-5 are given in Table 8. The reconstructed bulk composition in Table 7 was obtained by combining the compositions of individual phases (determined by electron and ion microprobe) in their modal proportions (as measured by point-counting).

The bulk REE pattern for 1623-5 as determined by INAA is shown in Fig. 14, along with the REE patterns of the two other forsterite-rich FUN inclusions CG-14 and TE (CLAYTON et al., 1984; WARK et al., 1987). 1623-5 is slightly enriched in heavy REEs (HREEs) over light REEs (LREEs) and has a large negative europium anomaly. Also shown on Fig. 14 is the bulk REE pattern of 1623-5 reconstructed from electron and ion microprobe data and modal proportions of phases. This reconstruction also yields a HREE-enriched pattern but is lower in overall abundance, has a greater enrichment of HREEs relative to LREEs, and has a much smaller negative europium anomaly. The higher REE content and large negative europium anomaly in the INAA bulk pattern is caused by the absence of melilite from that sample. The overabundance of fassaite in the INAA bulk pattern is also indicated by the high scandium content of the INAA

sample ( $\sim 60 \times \text{C1}$  chondrites).† It is not surprising that the INAA bulk sample is unrepresentative, as it consisted of only six grains.

The reconstructed bulk REE pattern of 1623-5 shows lower overall enrichment factors than those of CG-14 and TE; this is probably due to the higher proportion of olivine in 1623-5. WARK et al. (1987) previously noted that TE and CG-14 have HREE-enriched patterns; in order for 1623-5 to have a flat REE pattern, the melilite/pyroxene ratio would have to be 7 rather than the observed ratio of 1.7. The fact that now three forsterite-bearing inclusions have such patterns would seem to be a real characteristic of such inclusions and not a sampling bias. It seems unlikely that our sample of 1623-5 could be so unrepresentative and that the other two samples of forsterite-rich FUN inclusions could be unrepresentative in the same way.

The INAA analysis of 1623-5 shows that refractory siderophiles are enriched by 2.2–3.5  $\times \text{C1}$ . As these elements are likely to be contained mostly within very small metal-oxide-sulfide grains (presumably submicroscopic, as none were observed in a thorough SEM examination of the polished section), this bulk composition is probably more representative of the whole than in the case of the lithophile elements. TE and CG-14 have similarly low enrichment levels for the siderophile elements (CLAYTON et al., 1984; WARK et al., 1987), but only HAL has levels as low as these (DAVIS et al., 1982).

### Individual Phases

Of the primary igneous phases in the core of 1623-5, fassaite has the highest concentrations of trace elements: REE enrichments are 10–80  $\times \text{C1}$  (Fig. 15), and scandium, titanium, yttrium, zirconium, and niobium are highly enriched. The average REE pattern is characterized by a gradual increase in REE enrichment factor by a factor of 2 from lanthanum to samarium, a negative europium anomaly, and uniform enrichments in the HREEs at about the same level as samarium. The individual patterns are similar in shape, but vary by a factor of 5 in absolute concentration. The patterns become somewhat flatter with increasing REE concentration; fassaite in Allende coarse-grained Type B1 inclusions shows the same effect (MACPHERSON et al., 1989; DAVIS et al.,

† In this context,  $\times \text{C1}$  indicates enrichment factor relative to C1 chondrites and should not be confused with the refractory inclusion named C1.

Table 7. Bulk composition of Vigarano 1623-5. Oxide concentrations are given in wt% and element concentrations in ppm.

Element	INAA*	Reconstructed†
Na	<350	362
MgO	43.6 ± 1.3	35.7
Al <sub>2</sub> O <sub>3</sub>	5.56 ± 0.07	8.60
SiO <sub>2</sub>		39.3
Cl	<1200	
K	237 ± 33	40.8
CaO	8.16 ± 0.83	15.4
Sc	358.06 ± 0.08	85.3
TiO <sub>2</sub>	1.21 ± 0.08	0.884
V	146 ± 7	64.1 ± 3.6
Cr	215 ± 3	237
Mn	28.1 ± 8.3	14.7 ± 5.5
FeO	0.836 ± 0.012	0.107
Co	16.9 ± 0.8	
Ni	9320 ± 10	
Zn	71 ± 14	
As	2.40 ± 0.10	
Se	<0.12	
Br	29.3 ± 1.7	
Rb		0.778 ± 0.090
Sr	<25	96.4
Y		13.9
Zr	78 ± 15	35.5
Nb		0.845 ± 0.043
Mo	1.97 ± 0.35	
Ru	2.50 ± 0.16	
Sb	<0.39	
Cs	<0.10	
Ba	<110	1.08 ± 0.09
La	2.03 ± 0.05	1.08
Ce	6.38 ± 0.23	3.12
Pr		0.578
Nd		3.21
Sm	2.01 ± 0.01	1.17
Eu	<0.084	0.401
Gd		1.68
Tb	0.554 ± 0.022	0.311
Dy	2.38 ± 0.72	2.17
Ho	0.890 ± 0.066	0.493
Er		1.59
Tm	0.336 ± 0.046	0.259
Yb	2.81 ± 0.05	1.68
Lu	0.349 ± 0.015	0.257
Hf	4.40 ± 0.23	0.738 ± 0.042
Ta	0.200 ± 0.071	0.066 ± 0.020
W	<2.5	
Re	0.0831 ± 0.0059	
Os	1.40 ± 0.17	
Ir	1.618 ± 0.003	
Au	0.177 ± 0.003	
Th	0.200 ± 0.034	
U	<0.14	

\*INAA uncertainties are  $\pm 1\sigma$ , based on counting statistics; upper limits are  $<2\sigma$ . †The reconstructed bulk composition is calculated from modal proportions, electron microprobe oxide concentrations and ion microprobe element concentrations. Uncertainties are  $\pm 1\sigma$  and are only given when they exceed 5% of the amount present.

1990b). Fassaite has a remarkably wide range in scandium contents,  $10.2\text{--}168 \times C1$ . Scandium has a fassaite/liquid partition coefficient that is substantially greater than 1, so that early-formed fassaite is quite scandium-rich. Crystallization of fassaite rapidly depletes the liquid in scandium, so later-formed fassaites can have quite low scandium contents. For this reason scandium is useful as a measure of degree of fassaite crystallization. Plots of Sc vs. La, Y, and Zr (see DAVIS et al., 1990b) show that early-formed fassaite contains  $\sim 160 \times C1$  Sc,  $8 \times C1$  La, and  $30 \times C1$  Y, and the latest crystallized fassaite measured contains  $\sim 10 \times C1$  Sc,  $40 \times C1$  La, and  $80 \times C1$  Y. Zirconium decreases only slightly, from  $70$  to  $55 \times C1$ . The trace element zoning in 1623-5 fassaite

is similar to that in the Allende Type B1 inclusion TS-34 (DAVIS et al., 1990b).

Olivine is lower in REEs than the other major phases in the core of 1623-5, but has rather high REE concentrations for olivine. REE enrichment factors in olivine increase smoothly from  $<0.1$  for lanthanum to 3 for lutetium (Fig. 15). This type of HREE-enriched pattern has been observed in calcic olivine from the Angra dos Reis-like meteorite LEW 86010 (CROZAZ et al., 1988). Olivine formed in normal terrestrial, lunar, and meteoritic igneous environments typically has REE enrichments of  $<0.01 \times C1$ .

Melilite has variable concentrations of REEs. An average pattern representing 17 REE analyses of core melilite is shown in Fig. 16, along with the total range observed. The average REE pattern has enrichments that decrease smoothly from  $\sim 7 \times C1$  for lanthanum to  $\sim 3 \times C1$  for lutetium. At the upper limit of the range, one melilite spot has a REE enrichment that decreases smoothly from  $20 \times C1$  for lanthanum to  $12 \times C1$  for lutetium. Europium is enriched by  $30 \times C1$ . Seven melilite spots at the low end of the concentration range have LREEs at  $0.3\text{--}0.6 \times C1$ , europium at  $11\text{--}24 \times C1$ , yttrium at  $\sim 0.2 \times C1$ , and HREEs are below detection limits.

$\text{\AA}k_{95-99}$  melilite that has replaced olivine has REE patterns whose enrichment factors decrease by about a factor of 3 from lanthanum to lutetium, but with overall lanthanum enrichments ranging from 0.6 to 9; europium is uniformly enriched by  $21 \times C1$  (Fig. 17). The REE patterns of these melilite grains do not resemble those of the olivine that they have pseudomorphically replaced.

$\text{\AA}k_{40-60}$  melilite in the melilite mantle has a REE pattern (Fig. 18) similar to that of  $\text{\AA}k_{95-99}$  (Fig. 17), with lanthanum enrichments of  $2.4\text{--}3.4 \times C1$  and europium enrichments of  $13\text{--}17 \times C1$ . Several REE analyses were made of the melilite-perovskite intergrowth in the mantle overlying the pyroxene-rich portion of 1623-5 (Fig. 5); an average pattern is shown in Fig. 18. Compared to underlying fassaite, the gehlenite-perovskite intergrowth has a similar overall REE enrichment factor but a flatter REE pattern with all REEs except europium enriched by  $25\text{--}30 \times C1$ . Europium is enriched by only  $11 \times C1$ . The  $\text{\AA}k_{99}$  that pseudomorphically replaced olivine,  $\text{\AA}k_{40-60}$  in the melilite mantle, and the melilite-perovskite intergrowth are richer in barium than any of the interior phases (Table 8).

The porous mantle has a REE pattern (Fig. 17) that is similar to that of underlying fassaite but has no europium anomaly. The porous rim is quite high in barium; its enrichment is  $16\text{--}85 \times C1$ , while phases measured in the rest of the inclusion have enrichments of only  $<0.15\text{--}8 \times C1$ .

The smaller portion of 1623-5 contains a large area of olivine-free melilite, bounded on both sides by olivine-rich melilite (Fig. 1). Plotted on Fig. 10 is an electron microprobe step scan across this area; also plotted are several ion microprobe analyses for cerium and yttrium. From the edge to the center of the crystal, there is a monotonic change in melilite composition from  $\text{\AA}k_{89}$  to  $\text{\AA}k_{72}$ . This is the variation expected if this melilite crystallized from points Y and Z towards the spinel aggregate in the center. The partition coefficients for melilite in this composition range are low,  $0.05\text{--}0.1$  (KUEHNER et al., 1989; BECKETT et al., 1990); thus, the REE content should increase continuously towards the center of the grain.

Table 8. Major and trace elements in phases in Vigarano 1623-5, determined by ion microprobe. Oxide concentrations are given in wt% and element concentrations are given in ppm. Errors given are  $\pm 1\sigma$ , based on counting statistics, and are only given when they exceed 5% of the amount present; upper limits are  $<2\sigma$ .

	Melilite 1	Melilite 2	Melilite 3	Olivine	Fassaite	Åkermanite	Melilite Mantle	Melilite-Perovskite	Porous Mantle
MgO	11.1	12.3	11.5	52.3	13.6	13.1	7.61	9.52	13.9
Al <sub>2</sub> O <sub>3</sub>	7.92	6.20	7.93	0.780	14.2	1.90	16.3	15.9	14.7
SiO <sub>2</sub>	37.5	39.7	38.0	44.8	43.0	41.0	33.9	30.2	30.2
CaO	43.1	40.4	41.7	1.95	25.1	41.4	39.9	40.3	21.4
TiO <sub>2</sub>	0.0678	0.0911	0.286	0.0578	3.72	0.0702	0.227	2.90	5.50
FeO	0.130 ± 0.018	0.996	0.447 ± 0.028	0.062 ± 0.010	0.230 ± 0.024	2.19	1.37	0.527	12.4
Na	1153	1487	970	23.8	59.2	801	2591	3083	8874
K	49.1	165	68.5	10.4	40.6	185	130	233	1597
Sc	5.63 ± 0.61	7.92 ± 0.53	10.8 ± 1.3	40.2	402	6.73 ± 0.74	59.2	198	958
V	<11	6.8 ± 5.1	10.9 ± 5.7	49.5 ± 6.3	237	<5.9	30.9 ± 6.6	144 ± 8	335
Cr	51 ± 13	63 ± 15	55 ± 14	381 ± 33	159 ± 16	67 ± 15	29 ± 10	172 ± 11	162 ± 123
Mn	<33	81 ± 15	21 ± 17	<12	<48	354	46 ± 22	25 ± 20	634
Rb	1.33 ± 0.30	1.71 ± 0.29	2.98 ± 0.90	0.28 ± 0.12	1.24 ± 0.21	2.83 ± 0.52	3.33 ± 0.58	1.56 ± 0.47	12.9 ± 1.2
Sr	271	384	321	3.72 ± 0.28	46.5	379	226	246	211
Y	0.246 ± 0.071	4.90 ± 0.27	16.0 ± 1.2	2.53 ± 0.21	73.3	2.23 ± 0.26	3.60 ± 0.34	46.4	60.1
Zr	0.87 ± 0.22	4.74 ± 0.44	13.3 ± 1.8	0.24 ± 0.11	220	0.82 ± 0.26	10.5 ± 0.9	144	286
Nb	0.389 ± 0.079	0.91 ± 0.10	2.73 ± 0.43	0.214 ± 0.053	3.20 ± 0.17	0.69 ± 0.13	0.72 ± 0.13	5.72 ± 0.45	4.05 ± 0.32
Ba	1.80 ± 0.30	3.81 ± 0.36	4.00 ± 0.89	0.25 ± 0.10	0.93 ± 0.16	11.0 ± 0.9	9.47 ± 0.83	8.71 ± 0.95	94.0
La	0.242 ± 0.043	1.95 ± 0.10	3.78 ± 0.33	<0.022	4.38	0.799 ± 0.089	0.6360 ± 0.083	5.81 ± 0.29	3.54 ± 0.20
Ce	0.313 ± 0.086	3.42 ± 0.23	9.42 ± 0.92	0.068 ± 0.040	14.9	1.20 ± 0.19	1.45 ± 0.22	17.0 ± 0.9	10.0 ± 0.6
Pr	0.082 ± 0.024	0.546 ± 0.048	1.34 ± 0.18	0.021 ± 0.013	2.88	0.227 ± 0.045	0.295 ± 0.052	2.67 ± 0.18	2.32 ± 0.14
Nd	0.49 ± 0.10	2.35 ± 0.17	6.53 ± 0.67	0.060 ± 0.044	16.9	1.18 ± 0.18	1.04 ± 0.17	14.2 ± 0.7	12.1
Sm	0.064 ± 0.044	0.613 ± 0.053	1.47 ± 0.19	0.063 ± 0.036	6.31	0.425 ± 0.094	0.429 ± 0.069	5.13	5.27
Eu	0.892	1.35	1.41 ± 0.11	<0.016	0.564	1.17 ± 0.0	0.895 ± 0.056	0.653 ± 0.058	2.33
Gd	<0.14	0.90 ± 0.12	2.24 ± 0.41	0.060 ± 0.043	9.41	0.32 ± 0.13	0.47 ± 0.14	6.56 ± 0.55	6.03 ± 0.47
Tb	<0.028	0.1390 ± 0.021	0.322 ± 0.074	<0.016	1.79	0.042 ± 0.023	0.127 ± 0.028	1.13 ± 0.10	1.33 ± 0.09
Dy	<0.11	0.73 ± 0.10	2.08 ± 0.39	0.289 ± 0.068	12.0	0.178 ± 0.095	0.52 ± 0.13	7.63 ± 0.54	8.95 ± 0.49
Ho	0.072 ± 0.020	0.246 ± 0.028	0.290 ± 0.073	0.107 ± 0.020	2.50	0.052 ± 0.024	0.141 ± 0.032	1.46 ± 0.12	2.09 ± 0.12
Er	<0.10	0.5860 ± 0.072	1.55 ± 0.26	0.374 ± 0.055	8.21	<0.14	0.223 ± 0.079	4.22 ± 0.31	5.44 ± 0.30
Tm	<0.034	0.110 ± 0.018	0.209 ± 0.051	0.077 ± 0.013	1.28	<0.046	0.023 ± 0.021	0.699 ± 0.060	0.973 ± 0.064
Yb	<0.074	0.460 ± 0.066	1.85 ± 0.28	0.704 ± 0.074	7.69	0.123 ± 0.065	0.218 ± 0.077	4.28 ± 0.34	6.77 ± 0.34
Lu	0.035 ± 0.015	0.033 ± 0.014	0.168 ± 0.054	0.100 ± 0.017	1.24	0.047 ± 0.021	<0.040	0.598 ± 0.081	0.880 ± 0.080
Hf	0.196 ± 0.068	0.301 ± 0.074	<0.37	<0.086	4.50	0.59 ± 0.12	0.26 ± 0.11	2.90 ± 0.39	5.81 ± 0.42

Key: Melilite 1—Interior melilite, 7 analyses with low REE. Melilite 2—Interior melilite, 9 analyses with intermediate REE. Melilite 3—Interior melilite, 2 analyses with high REE. Olivine—6 analyses. Fassaite—8 analyses. Åkermanite—pseudomorphs after olivine, 4 analyses. Melilite Mantle—Åk<sub>40-60</sub>, 4 analyses. Melilite-Perovskite—intergrowth in mantle, 4 analyses. Porous mantle—7 analyses.

It is obvious from Fig. 10 that the situation is more complicated for this grain, as the REE contents are high near point Y, drop by factors of 30–40 halfway between point Y and the spinel, and increase again by factors of 30–40 near the spinel. It is clear from the REE profile that this olivine-free melilite area did not simply crystallize from a melt. It may represent mantle and interior melilite that has been sampled by the plane of the thin section in a complicated way.

## DISCUSSION

There are four separate questions concerning the genesis of 1623-5. (1) How did it acquire the nuclear anomalies in

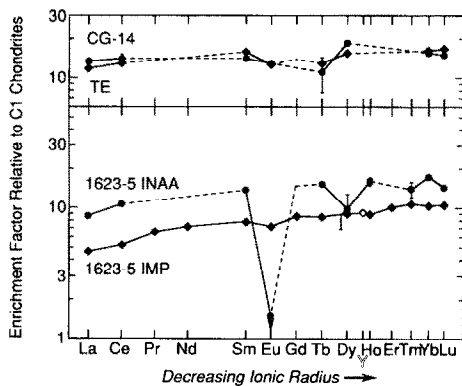


FIG. 14. INAA and reconstructed bulk REE abundance diagrams for 1623-5. Also shown for comparison are the bulk REE patterns for two other forsterite-bearing FUN inclusions, TE and CG-14.

its core? (2) How did it acquire the extreme mass-fractionation effects in the core, apart from any questions of how the mantle formed? (3) What is the relationship between the mantle and the core? And (4), how did the mantle form? The first of these questions will be considered in a separate paper (LOSS et al., in prep.); we address only the last three here.

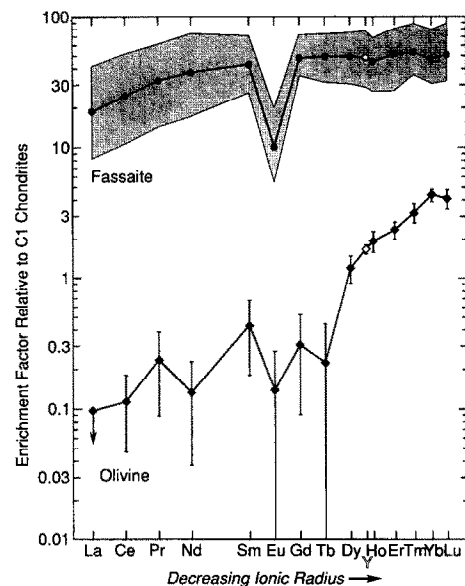


FIG. 15. Average REE patterns of olivine and fassaite from the core of 1623-5, with the range of fassaite compositions shaded.

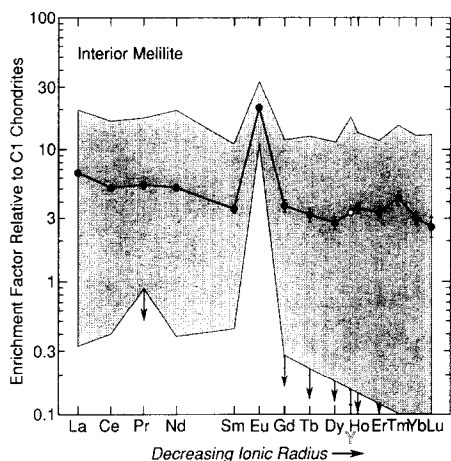


FIG. 16. Average and range of REE patterns for melilite from the core of 1623-5.

### Petrologic Constraints

The bulk composition of the core of the main portion of 1623-5 is highly forsterite-normative; plotted (Fig. 19) on a forsterite-anorthite-gehlenite projection from spinel (STOLPER, 1982), the core bulk composition falls in the forsterite primary phase field. As shown, a melt of this composition will crystallize spinel or olivine first, followed successively by melilite (when the liquid reaches point A in Fig. 19) and pyroxene (when the liquid reaches point B). Note that point B is a reaction point, at which olivine reacts with the melt to form melilite plus pyroxene. Depending on whether the melt is exhausted before the olivine has completely reacted, crystallization will terminate at either point B or point C.

If 1623-5 followed such a crystallization path, any olivines that became trapped within growing melilite crystals while the liquid evolved from point A to point B in Fig. 19 should have been protected against reaction at point B. The expected texture therefore would be euhedral olivines occurring only

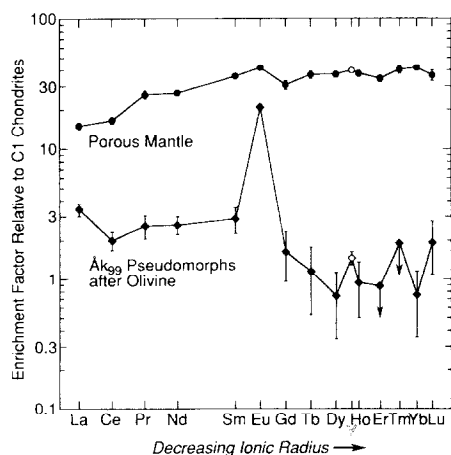


FIG. 17. Average REE patterns of  $\text{Åk}_{95-99}$  melilite that pseudomorphically replaces olivine in the mantle of 1623-5 and of porous mantle.

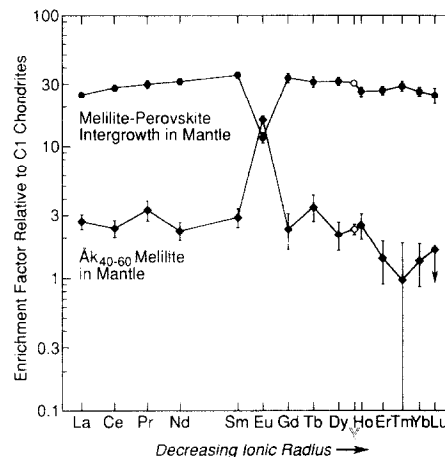


FIG. 18. Average REE patterns of melilite + perovskite intergrowths and of  $\text{Åk}_{40-60}$  mantle melilite in 1623-5.

inside early melilite and smaller, rounded and resorbed olivines everywhere else. This texture is not observed. Rather, euhedral olivines are found mostly inside pyroxene, as if *pyroxene* had started crystallizing prior to melilite. There are several possible explanations for this discrepancy; none is entirely satisfactory. The most obvious of these—that 1623-5 did not solidify from a melt—seems least likely. Despite the discrepancy in the crystallization sequence, the overall textures and the fact that there is a very well-defined crystallization sequence are suggestive of an igneous process. Moreover, the two semicircular embayments in 1623-5 are similar to structures observed in another forsterite-rich inclusion, ALVIN, and interpreted by MACPHERSON et al. (1981, 1985) to be vesicles trapped during the solidification of the melt from which ALVIN formed. If 1623-5 did solidify from a melt, the possible explanations for the discrepancy in predicted vs. observed crystallization sequence are as follows: (1) the interpretation of the observed textures is incorrect; (2) the thin section, used to obtain the point count from which the bulk composition is calculated, is not representative of the whole inclusion; or (3) the phase diagram is incorrect. The textures are simply too straightforward for (1) to be likely and (3) is ad hoc. The most probable explanation is a non-representative section, because the existing section samples only one-half of what is clearly a very heterogeneous inclusion.

The high calcium contents of the olivine place a constraint on the minimum temperature of the melt from which the olivine crystallized. Olivine in 1623-5 contains an average of 4.3 mol% monticellite component. On the 1 atm monticellite-forsterite binary (ADAMS and BISHOP, 1985), this composition implies a minimum quench temperature of 1150°C. At the other extreme, isotherms in the system gehlenite-anorthite-forsterite (STOPLER, 1982) indicate that the liquidus temperature of a melt having the composition of the core in 1623-5 might have been as great as 1600°C if the inclusion melted completely; the maximum temperature would be less if melting were incomplete.

However, even the most casual inspection of the distribution and compositions of phases in 1623-5 reveals that the core and mantle assemblages are so different from one another

as to be out of equilibrium. Specifically, the assemblage in the portions of the mantle that overlie core melilite,  $\text{Åk}_{40-60}$  melilite + spinel + hibonite, is suggestive of a far more aluminum-rich bulk composition than the fassaite +  $\text{Åk}_{89}$  melilite + forsterite assemblage in the core. Considering just the composition of the melilite with respect to phase relationships in the simple binary system gehlenite-åkermanite, the melilite in the core and mantle plot on opposite sides of the binary minimum at  $\text{Åk}_{72}$  (OSBORN and SCHAIRER, 1941). Although there may be a small shift in its composition, this minimum persists into systems containing anorthite and pyroxene (GEE and OSBORN, 1969). There is no simple way for a single homogeneous melt to crystallize melilite having compositions on both sides of the minimum during fractional crystallization. No fractional crystallization scheme involving phases present in the mineral assemblage of 1623-5 could cause the composition of the crystallizing melilite to cross this minimum. This incompatibility suggests that the mantle formed from a melt of *different composition* than the core. Yet, the isotopic compositions of the core and mantle are sufficiently similar and unusual that they are almost certainly related. The simplest model is one in which the mantle is derived from the core during some later event that leaves most of the core untouched, and the obvious process is volatilization.

A schematic illustration of how this volatilization might have occurred is shown in Fig. 19. We assume that in a relatively refractory melt having the bulk composition of the core of 1623-5, the most volatile species are  $\text{SiO}_2$  and  $\text{MgO}$  and that they evaporate at roughly comparable rates (HASHIMOTO, 1983). Two limiting cases are drawn, in which the  $\text{SiO}_2/\text{MgO}$  weight ratios are 0.65 and 0.82 (the ratio for forsterite is 0.75, that of the bulk inclusion is 1.08). In our model the starting bulk composition and the limiting cases are constrained by several petrographic observations. First, the sharp boundary between the mantle and core and the absence of any relict core phases in the mantle other than spinel indicate that the outer portion of the inclusion melted almost completely and volatilized without the core melting at all; thus, the starting composition that was volatilized was effectively bulk core and *not* the minimum melt composition at point B. An obvious implication of this is that the volatilization event was very fast. Second, the presence of melilite pseudomorphs after olivine at the core-mantle boundary suggests that the melt composition was driven across the melilite-olivine cotectic on Fig. 19. Finally, the absence of pyroxene and monticellite from the core-mantle boundary region indicates that the melt did not pass through the phase volumes of either of these two phases; this places limits on the  $\text{SiO}_2/\text{MgO}$  ratios (assumed to be constant during volatilization) permissible in the volatilizing species as shown on the diagram. The fact that the melilite replacing the olivine is  $\text{Åk}_{95-99}$  suggests that the actual trajectory was probably closer to the upper one ( $\text{SiO}_2/\text{MgO} = 0.65$ ), because liquids near point B will be in equilibrium with more magnesium-rich melilite than ones farther down the melilite-olivine cotectic (BECKETT, 1986). Although we have not extended the melt trajectory very far into the melilite primary phase volume, in fact the final melt must have been sufficiently aluminous to be in equilibrium with the  $\text{Åk}_{16-40}$  melilite found in parts of the mantle.

### Isotopic Constraints

It has long been known that the large isotopic mass fractionations observed in FUN inclusions such as 1623-5 could have been produced by Rayleigh-type volatilization, but without knowing the precise nature of the volatilizing species and the magnitudes of their isotopic fractionation factors it has not been possible to quantitatively evaluate such a model.

Recently, however, DAVIS et al. (1990a) investigated the isotopic mass fractionation of oxygen, magnesium, and silicon during laboratory evaporation of forsterite. They found that evaporation of solid forsterite produced little mass fractionation in the residue, but that evaporation of liquid  $\text{Mg}_2\text{SiO}_4$  produced substantial mass fractionation. The isotopic compositions of the melt residues follow a Rayleigh fractionation curve extremely well, with the gas/solid isotope fractionation factor closely approximating that predicted from the masses of the evaporating species Mg,  $\text{O}_2$ , and  $\text{SiO}_2$ . These experiments imply that it is necessary to melt the residue in order to produce large mass fractionations during evaporation, because subsolidus diffusion rates are too low to permit internal equilibration of solid residues during evaporation. The petrologic evidence suggests that the interior of 1623-5 was melted, but 1623-5 did not necessarily evaporate while molten. If evaporation did occur while the interior of 1623-5 was molten, it may have caused the large isotopic mass fractionations of oxygen, magnesium, and silicon.

In the DAVIS et al. (1990a) experiments, the degree of mass loss of oxygen, magnesium, and silicon was the same in each sample, because liquid  $\text{Mg}_2\text{SiO}_4$  evaporates congruently. The degree of mass loss of these three elements from the interior of 1623-5 can be calculated from the DAVIS et al. (1990a) gas/solid isotopic partition coefficients. For silicon, we use the bulk value,  $\delta^{30}\text{Si} = 20.26\%$ . For magnesium, we use the calculated magnesium isotopic composition of the interior,  $\Delta^{25}\text{Mg} = 30.6\%$  (Table 6). For both magnesium and silicon, we assume that the starting material had normal isotopic composition. For oxygen, two choices exist. If we extrapolate along a slope  $1/2$  line from the 1623-5 point to the CAI reference line in Fig. 13, the length of the line corresponds to an  $^{18}\text{O}$  fractionation of 23%. In previous experiments where mineral separates have been made of FUN inclusions (CLAYTON et al., 1984), the data for each FUN inclusion are displaced from the CAI reference line by different amounts but lie along a line that intersects the CAI reference line near the terrestrial mass-fractionation line. The most likely explanation for this behavior is that all of the FUN inclusions were mass fractionated away from the (-41, -40) point on the three isotope diagram and then later experienced partial isotopic exchange with the same isotopic reservoir as the normal CAIs. No oxygen isotopic analyses of mineral separates of 1623-5 have been made. If we assume that 1623-5 is similar to other FUN inclusions in its mass fractionation and isotopic exchange behavior, then a second method for calculating the degree of oxygen mass fractionation is to measure the length of a slope- $1/2$  line from the (-41, -40) point on the normal CAI reference line to an extension of a line passing through the 1623-5 point and the intersection of the terrestrial mixing and CAI reference lines. The length corresponds to an  $^{18}\text{O}$  fractionation of 29%.

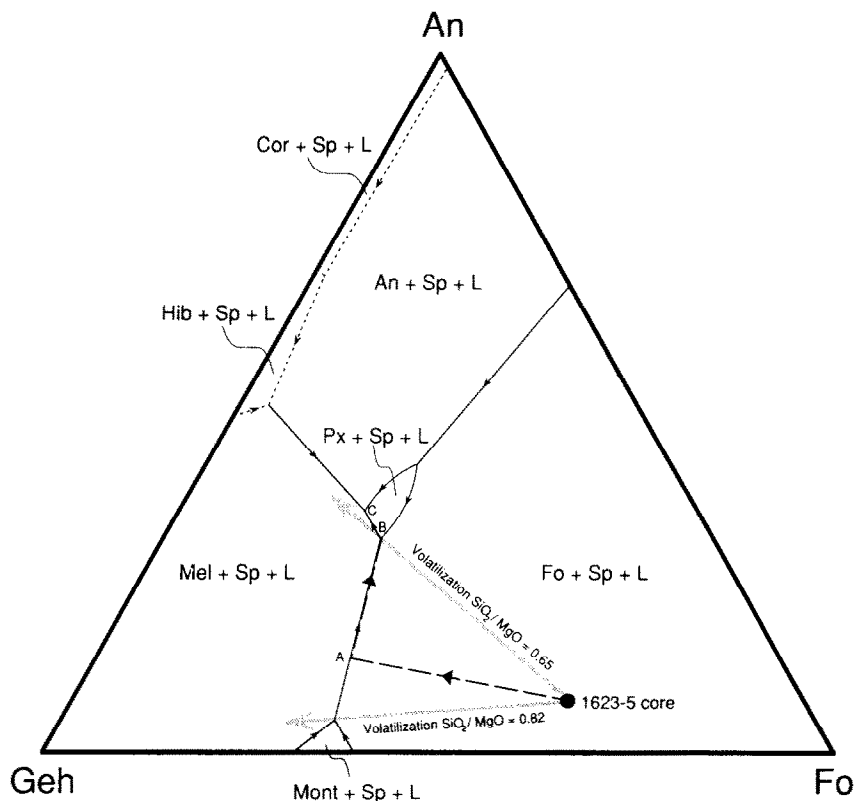


FIG. 19. Spinel projection of the CaO-MgO-SiO<sub>2</sub>-Al<sub>2</sub>O<sub>3</sub> system onto the plane gehlenite-forsterite-anorthite, showing the bulk composition of the fassaite-rich and melilite-rich portions of the core of 1623-5. Fractional crystallization of a melt having the composition of the fassaite-rich core will follow the trajectory indicated by the dashed arrow and ending at point B. The melilite-rich mantle is believed to have formed by volatilization of SiO<sub>2</sub> and MgO from such a melt by following a trajectory somewhere between the two shaded grey arrows. Further explanation is given in the text.

The percent residue calculated from the Rayleigh equation and the DAVIS et al. (1990a) data is 13% for magnesium, 24% for silicon, 30% for oxygen if oxygen exchange has not taken place, and 23% for oxygen if exchange has taken place. It seems unlikely that the degree of mass loss of oxygen was greater than that of magnesium and silicon so, in the context of a volatilization model, 1623-5 would necessarily have experienced oxygen isotope exchange with a normal reservoir in the same way as the other FUN inclusions (CLAYTON et al., 1984). It is possible that there was greater mass loss of magnesium than silicon, as the residue is unlikely to have evaporated congruently.

There are three possible difficulties with interpreting the origin of the mass fractionation in the interior of 1623-5 as being the result of melt volatilization. First, if the major element composition of the starting material was something like chondritic, then it had a very unusual oxygen isotopic composition relative to any known bulk chondrites; it would have plotted near the lower end of the Allende inclusion 3-isotope mixing line. There are materials of approximately chondritic composition that plot at this position on the 3-isotope oxygen diagram: one example is the forsterite-rich inclusion V1c (CLAYTON et al., 1987). Second, other forsterite-bearing inclusions are known that do not possess large mass-dependent isotope fractionations (e.g., CLAYTON et al., 1977; their sample Al6S3 and illustrated in their Fig. 5). Because

the fractionated and nonfractionated inclusions are otherwise very similar chemically and mineralogically, they must have formed by different processes that fortuitously converged on very similar products. The discovery of DAVIS et al. (1990a) that evaporation of forsterite just below the melting point produces little isotopic mass fractionation while evaporation of molten forsterite produces large mass fractionation provides a mechanism for producing chemically similar objects with very different degrees of isotopic fractionation. Finally, it is not clear why there is an association between large degrees of mass fractionation of oxygen, magnesium, and silicon and nuclear isotope anomalies in nearly every element measured among the FUN inclusions. One possibility is that the precursor to most refractory inclusions is isotopically heterogeneous, with individual components having some of the isotopic characteristics of the FUN inclusions. Other components in these precursors had isotope anomalies of opposite sign in amounts such that homogenization during melting and recrystallization produced a CAI with no detectable nuclear anomalies. If such a precursor were evaporated, some refractory phases carrying isotope anomalies might survive the evaporation event and leave a residue with mass-fractionated oxygen, magnesium, and silicon and isotopically anomalous refractory elements. Isotopic analyses of individual phases likely to be relict in normal CAIs would provide a test of such a model. So far, high-precision isotopic analyses

of mineral separates from normal CAIs and ion microprobe analyses of individual phases in CAIs have not revealed any heterogeneity in the distribution of nuclear isotope anomalies.

In spite of the above arguments, the large mass fractionation and the similarity of the amount of fractionation of oxygen, magnesium, and silicon to that produced in laboratory evaporation residues (DAVIS et al., 1990a) suggest that volatilization played a role in formation of the core of 1623-5. If the core itself is not a residue from a volatilization event, its precursor may have formed from a reservoir that already had the mass-fractionation signature from previous evaporation events in a poorly mixed portion of the solar system or in other stellar environments. Pushing the evaporation event back earlier also presents problems: the starting material for the evaporation must have the same isotopic composition as normal solar system material, i.e., normal magnesium and silicon and oxygen at the  $^{16}\text{O}$ -rich end of the CAI mixing line on the 3-isotope oxygen diagram.

It is also worth pointing out that, although the isotopic and bulk chemical composition of 1623-5 (and C1, EK1-4-1, CG-14 and TE) can be explained as the result of volatilization of a near-chondritic starting composition, such a process does not necessarily explain the isotopic and bulk compositions of most "normal" refractory inclusions. The latter are markedly more refractory in their bulk compositions and yet show much less isotopic mass fractionation (CLAYTON et al., 1988) than the three forsterite-rich FUN inclusions.

D. D. CLAYTON (1981) has suggested that the isotopic mass fractionation of oxygen, magnesium, and silicon in FUN inclusions arose through sputtering of tiny grains in the interstellar medium, but R. N. CLAYTON et al. (1984) present several convincing arguments that sputtering does not play a significant role in isotopic mass fractionation.

The mantle of 1623-5 gives a mixed signal with respect to isotopic mass fractionation during evaporation: melilite is not fractionated, but spinel and hibonite are. If the mantle around 1623-5 formed by later remelting and evaporation of the outer surface of the original inclusion, one might expect to see enrichment in the heavy isotopes of magnesium and silicon relative to the core. The measurements made on magnesium isotopes are more extensive than those on silicon isotopes and provide the major test of this expectation. As can be seen from Table 6, melilite in both the interior and the mantle has a uniform magnesium fractionation of 32‰/amu. The change in chemical composition of melilite implies a mass loss of at least 72% of the original magnesium. Using the DAVIS et al. (1990a) gas/solid partition coefficients, a magnesium fractionation of at least 20‰/amu *relative to interior phases* would be expected in mantle melilite. It is clear that the mass fractionation effects observed are much smaller. A similar case exists for the melilite-perovskite intergrowth that mantles the fassaite-bearing portions of the interior. Here, the magnesium isotopic composition is indistinguishable from that of the interior. Magnesium in the melilite-rich porous mantle overlying the melilite-perovskite area is isotopically lighter by 6‰/amu than the interior. Spinel found in mantle areas overlying both melilite- and fassaite-rich portions of the interior is significantly heavier (by 7‰/amu) than that in the interior. Two analyses show that hibonite at the extreme outer edge of the mantle has the largest magnesium fraction-

ation measured in this inclusion, 45‰/amu, 13‰ higher than the bulk interior. Using the DAVIS et al. (1990a) gas/solid partition coefficients, mass losses of 40 and 61% are calculated from the magnesium mass fractionation between the interior and spinel and hibonite, respectively.

Therefore, although the direction of isotopic mass fractionation in mantle spinel and hibonite relative to phases in the core is consistent with a volatilization origin for the mantle, the major phase in the mantle, melilite, does not show any isotopic fractionation relative to the interior. This disagreement of magnesium fractionation with degree of mass loss is not unique to 1623-5. Previous studies of several Type A inclusions from Allende, Vigarano, and Efremovka (DAVIS et al., 1986; LAUGHLIN et al., 1986; FAHEY et al., 1987) have shown that phases in the Wark-Lovering rims are isotopically nearly normal while phases in the interior are mass fractionated by as much as  $\sim 10\%$  in  $^{25}\text{Mg}$ ; as the rims are believed to have formed by volatilization (e.g., MACPHERSON et al., 1988), their present isotopic compositions are interpreted to be the result of reequilibration with the surrounding gaseous reservoir. This may have occurred in 1623-5. This is supported by the observation that the porous rim of 1623-5, which should have exchanged most easily, contains the isotopically lightest magnesium.

We conclude that the isotopic characteristics of the mantle relative to the core are suggestive of and qualitatively consistent with a model in which the mantle is derived from the core by volatilization, but there are quantitative inconsistencies for which we do not as yet have a completely satisfying explanation.

#### Trace Element Constraints

The REE patterns of the individual phases in the interior of 1623-5 are consistent with the interpretation that the core of 1623-5 was once molten; they are similar to patterns seen in the same phases in Type B CAIs whose igneous origin has been established on experimental grounds (STOLPER, 1982; MACPHERSON et al., 1984). Melilite has a LREE-enriched pattern with fairly low levels of all REEs except europium, typical of melilite from many other CAIs. The low levels of REEs are consistent with low-melilite/liquid-partition coefficients in magnesium-rich melilite (KUEHNER et al., 1989; BECKETT et al., 1990). Pyroxene has HREE-enriched patterns with negative europium anomalies. The REE pattern of olivine is also HREE-enriched, and its shape is similar to that calculated from the partition coefficients of MCKAY (1986) and COLSON et al. (1988).

There are two estimates of the amount of magnesium loss required to form the melilite mantle. To move from the bulk composition to the forsterite-melilite cotectic on Fig. 19,  $\sim 90\%$  of the MgO must be lost. The difference in magnesium isotopic composition between interior phases and rim spinel and hibonite indicates that only 40–60% loss of MgO occurred. Comparison of mantle trace element patterns with those of interior phases does not show the 3.5-fold increase in refractory element concentration expected from loss of 90% of the MgO. The most reasonable interpretation is that volatilization did not take place from a melt having the composition of bulk 1623-5, but rather from a partial melt that contained solid crystals of at least spinel and forsterite.

The magnesium and silicon isotopes were used to infer that the interior of 1623-5 must have lost ~80% of its mass in a volatilization event if the observed mass fractionations are due to volatilization. The smoothness of the REE patterns in 1623-5 suggests that REEs were not lost in such an event. Even europium, the most volatile REE, is only slightly depleted relative to neighboring REEs. The bulk composition of the starting material for the evaporation must have had REE enrichments (relative to C1 chondrites) that started at ~1 for lanthanum and increased smoothly to 2.7 for lutetium.

### CONCLUSIONS

Study of the Vigarano FUN inclusion 1623-5 reveals a complex history. The precursor material from which it formed contained nuclear isotopic anomalies; this material was melted and crystallized spinel, olivine, fassaite, and melilite. The precursor material may have obtained the mass-fractionated oxygen, magnesium, and silicon signature from earlier evaporation events in the solar system or stellar environments, or evaporation may have taken place while the inclusion was molten. Later flash heating of the forsterite-fassaite-rich inclusion produced a surface melt from which much of the silicon and magnesium were lost by volatilization while the interior was left untouched; the resulting mantle contains an aluminum-rich mineral assemblage grossly out of equilibrium with the interior assemblage and is isotopically mass fractionated in favor of the heavy isotopes of magnesium relative to the core.

Volatilization has been proposed previously to explain various features of refractory inclusions, including the melilite-rich mantles on Type B1 inclusions (e.g., KURAT et al., 1975) and rims on inclusions (e.g., BOYNTON and WARK, 1987), but detailed studies using the ion microprobe have failed to show the expected heavy isotope enrichment in B1 mantles (MACPHERSON et al., 1989) and inclusion rims (e.g., DAVIS et al., 1986; FAHEY et al., 1987). 1623-5 is the first object in which petrologic and isotopic properties unambiguously indicate the action of volatilization.

Finally, it seems worth amplifying a point made by CLAYTON et al. (1984) now that additional data are available: relative to other types of refractory inclusions, an unusually large proportion of forsterite-bearing inclusions are isotopically unusual. Of the nine well-studied examples (e.g., WARK et al., 1987; this study), three (CG-14 and TE from Allende, 1623-5 from Vigarano) have mass-fractionated oxygen + magnesium + silicon isotopes, one (1623-5) has nuclear isotopic anomalies in heavy elements, and two (VIc from Vigarano, Al6S3 from Allende) have bulk oxygen isotopic compositions that plot at the extreme <sup>16</sup>O-rich end of the Allende mixing line in contrast to other silicate-rich inclusions from CV3 meteorites (CLAYTON et al., 1977, 1984, 1987). We know of no reason why this group of inclusions should be so blessed with unusual members, but it seems clear that studies of additional forsterite-bearing inclusions will probably be very rewarding.

*Acknowledgments*—This work was supported by the National Aeronautics and Space Administration through grants NAG 9-111 (AMD), NAG 9-230 (GJM), NAG 9-51 (RNC), and NAG 9-54 (LG)

and the National Science Foundation through grant EAR 86-16255 (RNC). We thank G. W. Lugmair for helpful comments and A. S. Kornacki and C. Johnson for providing constructive reviews.

*Editorial handling:* D. W. G. Sears

### REFERENCES

- ADAMS G. E. and BISHOP F. C. (1985) An experimental investigation of thermodynamic mixing properties and unit-cell parameters of forsterite-monticellite solid solutions. *Amer. Mineral.* **70**, 714–722.
- BECKETT J. R. (1986) The origin of calcium-, aluminum-rich inclusions from carbonaceous chondrites: an experimental study. Ph.D. thesis, Univ. of Chicago.
- BECKETT J. R., SPIVACK A. J., HUTCHEON I. D., WASSERBURG G. J., and STOLPER E. M. (1990) Crystal chemical effects on the partitioning of trace elements between mineral and melt: An experimental study of melilite with applications to refractory inclusions from carbonaceous chondrites. *Geochim. Cosmochim. Acta* **54**, 1755–1774.
- BENCE A. E. and ALBEE A. L. (1968) Empirical correction factors for the electron microanalysis of silicates and oxides. *J. Geol.* **76**, 382–403.
- BOYNTON W. V. and WARK D. A. (1987) Origin of CAI rims—I. The evidence from the rare earth elements. *Lunar Planet. Sci. XVIII*, 117–118.
- CLAYTON D. D. (1981) Origin of Ca-Al-rich inclusions. II. Sputtering and collisions in the three-phase interstellar medium. *Astrophys. J.* **251**, 374–386.
- CLAYTON R. N. and MAYEDA T. K. (1977) Correlated oxygen and magnesium isotope anomalies in Allende inclusions, I: Oxygen. *Geophys. Res. Lett.* **4**, 295–298.
- CLAYTON R. N., ONUMA N., GROSSMAN L., and MAYEDA T. K. (1977) Distribution of the presolar component in Allende and other carbonaceous chondrites. *Earth Planet. Sci. Lett.* **34**, 209–224.
- CLAYTON R. N., MACPHERSON G. J., HUTCHEON I. D., DAVIS A. M., GROSSMAN L., MAYEDA T. K., MOLINI-VELSKO C., ALLEN J. M., and EL GORESY A. (1984) Two forsterite-bearing FUN inclusions in the Allende meteorite. *Geochim. Cosmochim. Acta* **48**, 535–548.
- CLAYTON R. N., MAYEDA T. K., MACPHERSON G. J., and GROSSMAN L. (1987) Oxygen and silicon isotopes in inclusions and chondrules from Vigarano. *Lunar Planet. Sci. XVIII*, 185–186.
- CLAYTON R. N., HINTON R. W., and DAVIS A. M. (1988) Isotopic variations in the rock-forming elements in meteorites. *Phil. Trans. Roy. Soc. London A325*, 483–501.
- COLSON R. O., MCKAY G. A., and TAYLOR L. A. (1988) Temperature and composition dependencies of trace element partitioning: Olivine/melt and low-Ca pyroxene/melt. *Geochim. Cosmochim. Acta* **52**, 539–553.
- CROZAZ G., LUNDBERG L. L., and MCKAY G. (1988) Rare earth elements (REE) in the unique achondrite LEW 86010. *Lunar Planet. Sci. XIX*, 231–232.
- DAVIS A. M. and MACPHERSON G. J. (1988) Further isotopic and chemical investigations of an isotopically heterogeneous Vigarano inclusion. *Meteoritics* **23**, 264–265.
- DAVIS A. M., TANAKA T., GROSSMAN L., LEE T., and WASSERBURG G. J. (1982) Chemical composition of HAL, an isotopically unusual Allende inclusion. *Geochim. Cosmochim. Acta* **46**, 1627–1651.
- DAVIS A. M., MACPHERSON G. J., and HINTON R. W. (1986) Rims revealed—ion microprobe analysis of individual rim layers in a Vigarano Type A inclusion. *Meteoritics* **21**, 349–351.
- DAVIS A. M., HASHIMOTO A., CLAYTON R. N., and MAYEDA T. K. (1990a) Correlated isotopic mass fractionation of oxygen, magnesium and silicon in forsterite evaporation residues. *Nature*, **347**, 655–658.
- DAVIS A. M., SIMON S. B., and GROSSMAN L. (1990b) Effective fassaite/liquid trace element distribution coefficients for Type B CAI's. *Lunar Planet. Sci. XXI*, 260–261.
- DOMINIK B., JESSBERGER E. K., STAUDACHER T., NAGEL K., and EL GORESY A. (1978) A new type of white inclusion in Allende:

- Petrography, mineral chemistry,  $^{40}\text{Ar}$ - $^{39}\text{Ar}$  ages, and genetic implications. *Proc. 9th Lunar Planet. Sci. Conf.*, 1249-1266.
- FAHEY A. J., ZINNER E. K., CROZAZ G., and KORNACKI A. S. (1987) Microdistributions of Mg isotopes and REE abundances in a Type A calcium-aluminum-rich inclusion from Efremovka. *Geochim. Cosmochim. Acta* **51**, 3215-3229.
- GEE K. H. and OSBORN E. F. (1969) Phase equilibria at liquidus temperatures in a part of the system  $\text{CaO-MgO-Al}_2\text{O}_3\text{-SiO}_2$ : The system  $\text{Ca}_2\text{MgSi}_2\text{O}_7\text{-Ca}_2\text{Al}_2\text{SiO}_7\text{-CaMgSi}_2\text{O}_6\text{-CaAl}_2\text{Si}_2\text{O}_8$ . *Bull. Earth Mineral Sci. Exp. Sta.*, 23-51.
- HASHIMOTO A. (1983) Evaporation metamorphism in the early solar nebula—evaporation experiments on the melt  $\text{FeO-MgO-SiO}_2\text{-CaO-Al}_2\text{O}_3$  and chemical fractionations of primitive materials. *Geochem. J.* **17**, 111-145.
- HINTON R. W. and BISCHOFF A. (1984) Ion microprobe magnesium isotopic analysis of plagioclase and hibonite from ordinary chondrites. *Nature* **308**, 169-172.
- HINTON R. W., DAVIS A. M., SCATENA-WACHEL D. E., GROSSMAN L., and DRAUS R. J. (1988) A chemical and isotopic study of hibonite-rich refractory inclusions in primitive meteorites. *Geochim. Cosmochim. Acta* **52**, 2573-2598.
- KUEHNER S. M., LAUGHLIN J. R., GROSSMAN L., JOHNSON M. L., and BURNETT D. S. (1989) Determination of trace element mineral/liquid partition coefficients in melilite and diopside by ion and electron microprobe techniques. *Geochim. Cosmochim. Acta* **53**, 3115-3130.
- KURAT G., HOINKES G., and FREDRIKSSON K. (1975) Zoned Ca-Al-rich chondrule in Bali: New evidence against the primordial condensation model. *Earth Planet. Sci. Lett.* **26**, 140-144.
- LAUGHLIN J. R., HINTON R. W., GROSSMAN L., and DAVIS A. M. (1986) Ion microprobe study of rim and core perovskite in an Allende inclusion. *Meteoritics* **21**, 430-431.
- LEE T., MAYEDA T. K., and CLAYTON R. N. (1980) Oxygen isotopic anomalies in Allende inclusion HAL. *Geophys. Res. Lett.* **7**, 493-496.
- LOSS R. D., LUGMAIR G. W., MACPHERSON G. J., and DAVIS A. M. (1990a) Isotope anomalies in Vigarano CAI's—hic et ubique. *Lunar Planet. Sci. XXI*, 718-719.
- LOSS R. D., LUGMAIR G. W., MACPHERSON G. J., and DAVIS A. M. (1990b) Isotopically distinct reservoirs in the early solar system. *Meteoritics* **25**.
- MACPHERSON G. J., GROSSMAN L., ALLEN J. M., and BECKETT J. R. (1981) Origin of rims on coarse-grained inclusions in the Allende meteorite. *Proc. 12th Lunar Planet. Sci. Conf.*, 1079-1091.
- MACPHERSON G. J., PAQUE J. M., STOLPER E., and GROSSMAN L. (1984) The origin and significance of reverse zoning in melilite from Allende Type B inclusions. *J. Geol.* **92**, 289-305.
- MACPHERSON G. J., HASHIMOTO A., and GROSSMAN L. (1985) Accretionary rims on inclusions in the Allende meteorite. *Geochim. Cosmochim. Acta* **49**, 2267-2279.
- MACPHERSON G. J., DAVIS A. M., LAUGHLIN J. R., and HINTON R. W. (1987) Isotopic heterogeneity in a forsterite-rich FUN inclusion. *Meteoritics* **22**, 451-453.
- MACPHERSON G. J., WARK D. A., and ARMSTRONG J. T. (1988) Primitive material surviving in chondrites: refractory inclusions. In *Meteorites and the Early Solar System* (eds. J. F. KERRIDGE and M. S. MATTHEWS), pp. 746-807. Univ. of Arizona Press.
- MACPHERSON G. J., CROZAZ G., and LUNDBERG L. L. (1989) The evolution of a complex Type B Allende inclusion: An ion microprobe trace element study. *Geochim. Cosmochim. Acta* **53**, 2413-2427.
- MAO X.-Y., WARD B., GROSSMAN L., and MACPHERSON G. J. (1990) Chemical compositions of refractory inclusions from the Vigarano and Leoville carbonaceous chondrites. *Geochim. Cosmochim. Acta* **54**, 2121-2132.
- MCKAY G. A. (1986) Crystal/liquid partitioning of REE in basaltic systems: extreme fractionation of REE in olivine. *Geochim. Cosmochim. Acta* **50**, 69-79.
- MOLINI-VELSKO C., MAYEDA T. K., and CLAYTON R. N. (1983) Silicon isotopes in components of the Allende meteorite. *Lunar Planet. Sci. XIV*, 509-510.
- OSBORN E. F. and SCHAIRER J. F. (1941) The ternary system pseudowollastonite-åkermanite-gehlenite. *Amer. J. Sci.* **239**, 715-763.
- PAPANASTASSIOU D. A. (1986) Cr isotopic anomalies in the Allende meteorite. *Astrophys. J.* **308**, L27-L30.
- STOLPER E. (1982) Crystallization sequences of Ca-, Al-rich inclusions from Allende: An experimental study. *Geochim. Cosmochim. Acta* **46**, 2159-2180.
- WARK D. A. and LOVERING J. F. (1982) The nature and origin of type B1 and B2 Ca-Al-rich inclusions in the Allende meteorite. *Geochim. Cosmochim. Acta* **46**, 2581-2594.
- WARK D. A., BOYNTON W. V., KEAYS R. R., and PALME H. (1987) Trace element and petrologic clues to the formation of forsterite-bearing Ca-Al-rich inclusions in the Allende meteorite. *Geochim. Cosmochim. Acta* **51**, 607-622.